International Journal of Plasticity 190 (2025) 104351

Contents lists available at ScienceDirect

International Journal of Plasticity

journal homepage: www.elsevier.com/locate/ijplas

Enhanced Strain Gradient Crystal Plasticity theory: Evolution of the length scale during deformation

Amirhossein Lame Jouybari [a,b,*], Samir El Shawish [a], Leon Cizelj [a,b]

[a] Jožef Stefan Institute, Jamova cesta 39, Ljubljana, Sl-1000, Slovenia
[b] University of Ljubljana, Jadranska ulica 19, Ljubljana, Sl-1000, Slovenia

ARTICLE INFO

Keywords:
Shear band
Grain boundary
Polycrystalline material
Fast Fourier transform method

ABSTRACT

An Enhanced Strain Gradient Crystal Plasticity (Enhanced-SGCP) theory, based on the quadratic energy contribution of the Nye tensor, is developed within a thermodynamically consistent framework to accurately capture shear band formation in terms of slip and kink bands within the microstructure. The higher-order modulus in the theory is intrinsically linked to the evolving microstructural properties during applied loading, introducing a physical length scale that governs shear band formation and evolution. It is demonstrated that the Classical-SGCP model (a Gurtin-type nonlocal theory) leads to an increasing width of localization bands, which eventually disappear, resulting in homogeneous deformation within the microstructure. This effect arises from the excessive annihilation of geometrically necessary dislocations, which suppresses localization and may lead to physically meaningless results in the formation of shear bands. To address this issue, the proposed Enhanced-SGCP theory effectively preserves the shear band width and maintains localization throughout the loading process by reducing the higher-order modulus associated with the sweeping away of hardening defects and local softening mechanism. Furthermore, the theory establishes a direct link between lattice curvature in kink bands and the Nye tensor, demonstrating that the kink bands transform into slip bands. Consequently, the Enhanced-SGCP theory breaks the equivalence between slip and kink bands, providing a more accurate physical representation of strain localization mechanisms in irradiated materials.

To computationally solve the governing balance equations, a fixed-point algorithm based on the fast Fourier Transform (FFT) method is developed. To validate the algorithm, an analytical solution for the Enhanced-SGCP theory is derived. High-resolution single-crystal simulations confirm that the kink bands transition into regularized slip bands through different physical length scales within the proposed Enhanced-SGCP framework. Furthermore, high-resolution simulations are performed on two-dimensional and three-dimensional polycrystalline aggregates, considering different length scales and various higher-order interface conditions at the grain boundaries. The results reveal that the strain gradient effects during applied loading are saturated and stabilized by the Enhanced-SGCP theory, ensuring sustained localization.

These findings highlight the capability of the proposed Enhanced-SGCP theory and the developed FFT-algorithm to provide a robust and physically consistent framework for modeling strain localization in crystalline materials. The proposed model offers significant improvements over classical approaches, particularly in preserving localization phenomena and accurately describing the interplay between slip and kink bands.

---

[*] Corresponding author at: Jožef Stefan Institute, Jamova cesta 39, Ljubljana, Sl-1000, Slovenia.
E-mail address: Amirhossein.Lame@ijs.si (A. Lame Jouybari).

https://doi.org/10.1016/j.ijplas.2025.104351
Received 18 February 2025; Received in revised form 14 April 2025

Nomenclature

γ_{cum}^{α}	Cumulative shear strain associated to each slip system	π	Pi number
τ_{cr}^{α}	Critical resolved shear stress associated to each slip system	θ	Rotation field
χ^{α}	Back-stress associated to each slip system	$\underset{\sim}{\alpha}$	Nye tensor
$\varGamma^{\alpha}$	Generalized back-stress associated to each slip system	ψ	Free energy
$\dot{\gamma}_{cum}^{\alpha}$	Rate of cumulative shear strain associated to each slip system	n	Norton flow exponent
$\dot{\gamma}^{\alpha}$	Rate of shear strain associated to each slip system	k	Norton flow coefficient
$\left(\nabla\dot{\underline{u}}\right)^{\mathrm{p}}$	Rate of the plastic distortion tensor	$\underset{\approx}{G}$	Green operator
$\overline{\nabla\underline{u}}$	Average part of the displacement gradient tensor	$\underset{\sim}{\tau}$	Polarization tensor
$\nabla\underline{u}^{\star}$	Fluctuation part of the displacement gradient tensor	ρ	Density of body
ψ^{h}	Free energy according to the hardening	j	Imaginary complex unit
$\triangle\tau^{\alpha}$	Maximum softening parameter	γ_0	Softening rate parameter
τ_0^{α}	Initial critical resolved shear stress	$\varLambda_0$	Length scale
D^{α}	Lattice residual dissipation associated to each slip system	$\underline{t}$	Cauchy traction vector
D^{tot}	Total lattice residual dissipation	$\underset{\approx}{\epsilon}$	Levi-Civita tensor
τ^{α}	Resolved shear stress associated to each slip system	$\overset{\times}{\underline{\omega}}$	Axial vector
$\varOmega^{\alpha}$	Dissipation potential associated to each slip system	f^{α}	Schmidt yield function
γ_{cum}^{tot}	Total cumulative shear strain	A^{α}	Higher order modulus
$\underline{n}^{\alpha}$	Normal vector to slip plane	$\underline{m}^{\alpha}$	Slip direction vector
$\underset{\approx}{C}^{0}$	Reference isotropic linear elasticity tensor	$\underset{\approx}{C}$	Elasticity tensor
$\underset{\sim}{\omega}$	Skew-symmetric part of displacement gradient tensor	$\underset{\sim}{R}$	Rotation tensor
$\left(\nabla\underline{u}\right)^{p}$	Plastic distortion tensor	$\underline{u}$	Displacement vector
$\nabla\underline{u}^{tot}$	Total displacement gradient tensor	$\left(\nabla\underline{u}\right)^{e}$	Elastic distortion tensor
$\underset{\sim}{\kappa}$	Lattice curvature tensor	$\mathcal{B}$	Body
$\partial\mathcal{B}$	Boundary of the body	N_g	Number of grains
$\underset{\sim}{\sigma}$	Cauchy stress tensor	$\underset{\sim}{s}$	Micro-stress tensor
$\underset{\sim}{M}$	Double-stress tensor	$\underset{\sim}{m}$	Double-traction tensor
$\underline{n}$	Outward normal vector to the plane	$\underset{\sim}{\varepsilon}^{e}$	Elastic strain tensor
$\underset{\sim}{F}$	Deformation gradient tensor	$\underset{\sim}{U}$	Right stretch tensor
$\underline{\xi}$	Frequency vector in Fourier space	$\underline{x}$	Position vector
L	Length of the microstructure	GS	Mean grain size
$\mathcal{IFFT}$	Inverse Fast Fourier transform	$\mathcal{FFT}$	Fast Fourier transform
Enhanced-SGCP	Enhanced Strain Gradient Crystal Plasticity	CCP	Classical Crystal Plasticity
Classical-SGCP	Classical Strain Gradient Crystal Plasticity	SGP	Strain Gradient Plasticity
GND	Geometrically necessary dislocation	SSD	Statistically stored dislocation

1. Introduction

Continuous media in solid mechanics can be broadly classified into simple and non-simple materials. Simple materials, such as the classical Cauchy continuum, are characterized by their response depending solely on the local state of deformation. In contrast, non-simple materials incorporate additional degrees of freedom or higher gradient, which enrich their description and behavior. These materials are further categorized based on the complexity of their formulation. When the additional degrees of freedom are introduced, as in Cosserat and micromorphic theories, they are referred to as higher-order continua. If the gradients of internal variables are also considered in defining the material's behavior, the material is classified as higher-grade media. These advanced models are typically associated with intrinsic length scales that arise from the underlying microstructure, allowing them to capture length scale-dependent mechanical behavior that cannot be explained by classical theories. A particularly significant example of such models is strain gradient plasticity (SGP), where the plastic part of the deformation is treated as a gradient of an internal variable. This approach enables the description of material behavior at microscopic scales, bridging the gap between microstructural effects and macroscopic observations, and provides a robust framework for understanding phenomena like length scale-dependent hardening and strain localization. The concept of enriching conventional plasticity with a material length scale parameter was first introduced to incorporate the plastic strain gradient term within the yield function, laying the foundation for first SGP theory (Aifantis, 1984). Building on this, a J_2-deformation version of SGP was developed to capture both strain hardening and strain gradient hardening effects, and the J_2-flow theory version of SGP was designed to model the elastoplastic behavior of solids (Fleck and Hutchinson, 1997). To ensure consistency with thermodynamic principles, SGP theories have been extended by introducing higher-order stresses conjugate to the strain gradient variables, applicable to both irrotational and rotational plastic flows (Gudmundson, 2004; Gurtin and Anand, 2005). Further refinements include the development of implicit gradient plasticity theories to address numerical challenges, such as those arising at moving elastoplastic boundaries. Additionally, the mechanism-based strain gradient plasticity theory, derived from a multiscale framework, establishes a direct connection between microscopic dislocation mechanisms and macroscopic plasticity (Gao et al., 1999).

The classical crystal plasticity theory provides a foundational framework for understanding the hardening behavior of materials, linking internal variables to scalar dislocation densities. In this framework, plastic deformation is conceptualized as the macroscopic outcome of dislocation glide, multiplication, and annihilation. However, this approach struggles to account for length-scale-dependent phenomena observed at smaller scales (Lindroos et al., 2022a; Agius et al., 2022; Hassani et al., 2025), such as those experimentally reported by (Hall, 1951; Petch, 1953) and commonly known as the *Hall-Petch* effect. This effect highlights the strengthening of materials with decreasing grain size, emphasizing the need for length-scale-dependent plasticity models. Length-scale-dependent plasticity becomes particularly critical when the size of modeled constituents approaches the characteristic lengths associated with underlying plastic deformation mechanisms, such as shear bands, dislocation interactions, and grain boundary effects. The physical basis for incorporating length scales into plasticity models is rooted in distinguishing dislocations into statistically stored dislocations (SSDs) and geometrically necessary dislocations (GNDs). The concept of GNDs, initially introduced by (Nye, 1953), directly links the concentration of GNDs to the curvature of the crystal lattice, providing a foundation for strain gradient-dependent material behavior (Kröner, 1962). Building on these insights, the Nye tensor became a cornerstone of strain gradient crystal plasticity (SGCP) theory. This framework, proposed by (Gurtin, 2002), incorporates the Nye tensor into the crystal energy density, enabling a more rigorous description of the interplay between strain gradients and dislocation mechanisms. Typically, the length scale in various SGP models is treated as a fixed material parameter during deformation. However, its magnitude can vary significantly across models, differing by several orders of magnitude (Liu and Dunstan, 2017). Experimental studies on microbending and microtorsion (Voyiadjis and Abu Al-Rub, 2005) have substantiated the hypothesis that different microstructural properties influence the magnitude of the length scale during deformation. These studies reveal that strain gradient effects are most pronounced during the initial stages of deformation but diminish as deformation progresses, suggesting that microstructural changes reduce size effects over time. Consequently, the length scale should not be treated as a fixed parameter but rather as one that evolves with deformation-dependent microstructural properties. Specifically, it is speculated that the length scale decreases as the plastic part of deformation increases, eventually saturating at higher levels of deformation. Consequently, the length-scale parameter in strain gradient plasticity is not constant but deformation-dependent, governed by the accumulation of plastic strain and evolving microstructural properties. This dynamic behavior underscores the need for advanced models that can accurately account for the variability of length scales throughout the deformation process.

Strain localization is a direct consequence of heterogeneous plastic deformation in crystalline materials, manifesting in phenomena such as necking, shear bands, and Lüders bands (Ren et al., 2021). Among these, shear bands are particularly significant as they result from material instability, often accompanied by softening behavior, and are experimentally recognized as a length-scale-dependent phenomenon. The isothermal shear bands are typically classified as slip bands (parallel to the slip plane) and kink bands (perpendicular to the slip plane), based on the pioneering work of (Asaro and Rice, 1977). Their classification was derived through a theoretical bifurcation analysis of crystals equipped with a single slip system, providing a foundational understanding of their behavior. In both slip and kink bands, intense dislocation glide occurs; however, their key distinction lies in their kinematics. Kink bands induce strong lattice rotations and high lattice curvatures, driven by the GNDs, which are not prominent in slip bands. Additionally, kink bands are known to accumulate significant strain incompatibility, particularly when an insufficient number of slip systems are active to facilitate dislocation glide. Experimental observations further reveal that the structure of kink bands often includes a dense distribution of short slip bands oriented perpendicular to the slip plane. Despite these statements, slip bands are predominantly observed in the microstructure of real materials, highlighting their significance in the context of shear band formation. Shear bands are also widely observed in the microstructures of irradiated materials, where their formation is a direct consequence of irradiation-induced damage. Irradiation introduces profound changes to the material's microstructure, which in turn affects its macroscopic mechanical properties. These effects include a loss of toughness, an increase in yield stress, and reductions in both ductility and the work-hardening domain.

Numerous studies have explored computational modeling of shear bands in crystalline materials, focusing on the formation and evolution of these localized deformation features. Classical crystal plasticity models, rooted in dislocation-based softening behaviors, have been extensively used to simulate strain localization (Hure et al., 2016; Patra and McDowell, 2016; Marano et al., 2019; Prakash et al., 2021; Ahmadikia et al., 2021; Clayton, 2022, 2024; Hestroffer et al., 2023; Lame Jouybari et al., 2023). These models successfully reproduce slip and kink bands, treating them as equivalent bifurcation modes, as established in the pioneering work of (Asaro and Rice, 1977). However, in reality, slip bands are more likely to form than kink bands, making the assumption of equivalence a significant limitation. Another major drawback of classical models lies in their mesh dependency. The simulations often suffer from the loss of ellipticity in the governing constitutive equations, leading to numerical instability. Various studies have attempted to address these computational issues. One prominent approach involves SGP, which introduces length scales into continuum media to act as a regularization mechanism for strain localization. For example, (Wulfinghoff et al., 2013) proposed a strain gradient crystal plasticity model based on the total cumulative shear strain, which effectively regularized strain localization. Building on this, (Ling et al., 2018) developed a reduced micromorphic single crystal plasticity model for voided-irradiated crystalline materials, also based on the total cumulative shear strain, to address localization problems, (Lindroos et al., 2022b) to regularize damage, (Scherer et al., 2021) simulation of the crack propagation, and (Phalke et al., 2022a) to reproduce adiabatic shear banding. Further advancements include the work of (Lame Jouybari et al., 2024), who introduced a strict microslip strain gradient crystal plasticity model based on the cumulative shear strain associated to each slip system. This model successfully regularized both slip and kink bands, accounted for size effects, and provided voxel-independent (mesh-independent) results for strain localization in irradiated crystalline materials. Despite these improvements, these models were unable to break the equivalence ratio between slip and kink bands, as they did not account for physical mechanisms distinguishing the two. An alternative perspective is offered by Cosserat crystal plasticity theory, which explicitly incorporates elastoplastic lattice torsion-curvature (Forest, 1998). This theory demonstrates, through bifurcation analysis, that the formation of kink bands can occur later than slip bands, and that kink band localization may be superseded by slip bands that do not induce lattice curvature. These findings affirm the importance of considering lattice curvature to break the equivalence ratio between slip and kink bands in crystalline materials.

Lattice curvature is intrinsically linked to the GNDs, as described by the Nye tensor (Nye, 1953). This tensor provides a physical characteristic that can be used to distinguish kink bands in the microstructure. Several studies, such as those by (Gurtin, 2002; Clayton et al., 2004; Phalke et al., 2022b; Pai et al., 2022; Demir et al., 2023), have incorporated the Nye tensor into strain gradient crystal plasticity models. Notably, (Marano et al., 2021) reported that by treating the Nye tensor as a strain gradient variable, kink bands could be suppressed in favor of slip bands, aligning with experimental observations for irradiated stainless steels. This highlights the potential of using the Nye tensor within strain gradient frameworks to capture and regulate shear band formation more realistically. Despite significant advancements, most strain gradient crystal plasticity (SGCP) models treat the length scale as a fixed parameter that does not evolve during deformation. This assumption overlooks the fact that the true nature and evolution of the length scale in real materials remain unclear. For instance, (Zbib and Aifantis, 1998) demonstrated that in a strain gradient framework with parabolic hardening and softening behavior, such as a gradient-dependent constitutive equation for flow stress, the width of slip bands narrows progressively during deformation. This observation has inspired further developments in continuum damage mechanics, where a damage-dependent length scale has been introduced to address the spurious spreading of damage width. Techniques such as micromorphic and integral non-local models have been applied to this problem by (Poh and Sun, 2017; Vandoren and Simone, 2018). Based on these ideas, (Dahlberg and Boasen, 2019) extended SGP theory to allow the intrinsic length scale to evolve during deformation. The study derived a physically motivated evolution equation for the length scale, directly linking it to dislocation density in materials subjected to bending. Similarly, (Petryk and Stupkiewicz, 2016) developed a model incorporating slip-rate gradients into the internal length scale, proposing a minimal gradient-enhanced crystal plasticity framework. (Ryś et al., 2022) introduced a Cosserat crystal plasticity model based on the accumulated rotation field in the spherical indentation of a copper single crystal. Additionally, (Scherer et al., 2019) introduced a micromorphic crystal plasticity model based on total cumulative shear strain, which effectively bounded localization bands and suppressed fictitious spreading in single irradiated crystals. According to that study, (Abatour and Forest, 2024) reported that classical scalar-based SGP models exhibit certain limitations. These include unbounded hardening behavior under static loading and cyclic hardening in bending, strain localization band propagation in softening materials, and the potential vanishing of the yield stress when the Laplacian term in the model becomes excessively large. To address these limitations, a strain gradient plasticity framework incorporating saturating variables has been proposed in (Abatour and Forest, 2024). While these advanced SGCP models offer improvements over classical formulations, further generalization is necessary, particularly for shear bands applications in polycrystalline materials. One key limitation is that these models rely on scalar internal variables or cumulative shear strain, which fail to account for lattice rotation and merely approximate the Nye tensor. Moreover, incorporating this internal variable within SGCP theory results in generalized stresses affecting both slip and kink bands in a similar manner, thereby failing to differentiate their relative influence in polycrystalline materials. Additionally, the role of grain boundaries in the transmission of shear bands remains unaddressed in these advanced formulations, therefore, highlighting the need for further theoretical developments.

This study introduces a novel Enhanced Strain Gradient Crystal Plasticity (Enhanced-SGCP) theory, based on the Nye tensor, which is rigorously derived within a thermodynamic framework. A key innovation is in demonstrating how the length scale evolves and eventually saturates during deformation or under applied loads, achieved by explicitly linking the higher-order modulus to the microstructural properties of irradiated materials. This approach is particularly relevant for understanding shear band formation in irradiated materials influenced by grain boundaries, as it captures their evolution through the combined effect of back-stress and generalized back-stress. In addition, the study establishes a Fast Fourier Transform (FFT) method to solve the governing balance equations more efficiently. Specifically, the classical balance equation (or linear momentum balance equation) is explicitly coupled with the generalized balance equation from the Enhanced-SGCP theory, enabling a robust numerical framework within in-house code (Matlab, 2022). By considering the two-dimensional and three-dimensional microstructures at high resolutions, the study provides comprehensive insights into the interplay between microstructural features and the evolving length scale, offering a novel perspective on strain localization phenomena in irradiated materials.

The structure of this paper is as follows. Section 2 consists of multiple subsections, where the thermodynamically consistent derivation of the Enhanced-SGCP theory is fully introduced in Section 2.1. The differences between the proposed Enhanced-SGCP theory and the Classical-SGCP theory (a Gurtin-type nonlocal theory) are detailed in Section 2.2. Additionally, Section 2.4 provides a comprehensive description of the developed FFT method, along with the pseudocode for the FFT algorithm. Section 3 presents the results obtained in this study, focusing on the investigation of the proposed Enhanced-SGCP theory through high-resolution single-crystal simulations, as well as two-dimensional and three-dimensional high-resolution polycrystalline simulations. This includes the development of an analytical solution, the effects of length scale and material properties, the role of grain boundaries, and the advantages of the proposed Enhanced-SGCP theory. Finally, Section 5 summarizes the conclusions of this study.

The notation used in this study includes scalar, first-order (vector), second-order, third-order, and fourth-order tensors represented as X, $\underline{X}$, $\underset{\sim}{X}$, $\underset{\simeq}{X}$, and $\underset{\approx}{X}$, respectively. The Levi-Civita third order permutation tensor is denoted by $\underset{\simeq}{\epsilon}$. Superscripts $^{\mathrm{tot}}$, $^{\mathrm{e}}$, $^{\mathrm{p}}$, $\dot{}$, $\hat{}$, *, and $^{-}$ are utilized to signify the total, elastic, plastic, time derivative, Fourier transform, fluctuation, and spatial mean value part of the tensor, respectively. Additionally, mathematical symbols such as $\otimes$, $\times$, $*$, $.$, $:$, ∇, $\nabla\,.$, $\nabla\times$, and Δ denote the tensor product, cross product, convolution, dot product, double contraction, gradient, divergence, curl and Laplacian operators. For example the curl of the second order tensor is calculated as $\nabla \times \underset{\sim}{X} = \epsilon_{jms} X_{im,s} \underline{e}_i \otimes \underline{e}_j$ in the Cartesian coordinate basis which is denoted as $(\underline{e}_1, \underline{e}_2, \underline{e}_3)$, and the Einstein's summation convention is used in indicial representations. Furthermore, the norm of the second order tensor is calculated as $\| \underset{\sim}{X} \| = \sqrt{\underset{\sim}{X} : \underset{\sim}{X}}$, and the symmetric and skew-symmetric parts of the second order tensor are calculated as $\mathrm{Sym}(\underset{\sim}{X}) = (\underset{\sim}{X} + \underset{\sim}{X}^T)/2$, and $\mathrm{Skew}(\underset{\sim}{X}) = (\underset{\sim}{X} - \underset{\sim}{X}^T)/2$.

2. Material and methods

This section introduces the Enhanced-SGCP theory based on the Nye tensor, focusing on its thermodynamically consistent derivation and the incorporation of a length-scale evolution as a function of microstructural properties of irradiated materials. To achieve these objectives, the principle of virtual power is combined with the Clausius–Duhem inequality, ensuring that the theory remains fully consistent with the laws of thermodynamics.

2.1. *Enhanced-SGCP: Evolution of length scale during deformation*

To model the fundamental slip mechanisms in a Face-Centered Cubic (FCC) crystal lattice, this study considers $\mathcal{N} = 12$ slip systems, $\left(\underline{m}^\alpha, \underline{n}^\alpha\right)$, represented by Miller indices as $\left\{111\right\}\langle 110\rangle$. Within the infinitesimal deformation framework, the total displacement gradient tensor is additively decomposed into its elastic and plastic parts, as shown in Eq. (1). In crystal plasticity, the elastic strain (Eq. (2)) captures the crystal's distortion, while the plastic part of the deformation (Eq. (3)) arises from dislocation glide.

$$\nabla \underline{u}^{\mathrm{tot}} = \left(\nabla \underline{u}\right)^{\mathrm{e}} + \left(\nabla \underline{u}\right)^{\mathrm{p}} \tag{1}$$

$$\underset{\sim}{\varepsilon}^{\mathrm{e}} = \tfrac{1}{2}\left(\left(\nabla \underline{u}\right)^{\mathrm{e}} + \left(\nabla \underline{u}\right)^{\mathrm{eT}}\right) \tag{2}$$

$$\left(\dot{\nabla} \underline{u}\right)^{\mathrm{p}} = \sum_{\alpha}^{\mathcal{N}} \dot{\gamma}^\alpha \underline{m}^\alpha \otimes \underline{n}^\alpha \tag{3}$$

To further account for the history-dependent nature of plastic flow, two additional positive-definite variables are introduced: the cumulative shear strain associated with each slip system (Eq. (4)) and the total cumulative shear strain (Eq. (5)). Additionally, the elastic component of the displacement gradient tensor from Eq. (1) is utilized to define the lattice rotation angle ($\theta = \| \overset{\times}{\underline{\omega}} \|$) by associating it with the axial vector $\overset{\times}{\underline{\omega}}$, derived from the skew-symmetric part of $\left(\nabla \underline{u}\right)^{\mathrm{e}}$. For small lattice rotation angles $|\theta| \ll 1$, within a coordinate basis $\left(\underline{e}'_1, \underline{e}'_2, \underline{e}'_3\right)$ where $\underline{e}'_3$ is aligned with the rotation axis, the skew-symmetric part of $\left(\nabla \underline{u}\right)^{\mathrm{e}}$ can be approximated by Eq. (6). Further details are provided in Appendices A and B.

$$\gamma^{\alpha}_{cum} = \int_0^{\mathrm{t}} \left|\dot{\gamma}^\alpha\right| d\mathrm{t} \tag{4}$$

$$\gamma^{tot}_{cum} = \sum_{\alpha}^{\mathcal{N}} \int_0^{\mathrm{t}} \left|\dot{\gamma}^\alpha\right| d\mathrm{t} \tag{5}$$

$$\mathrm{Skew}\left(\left(\nabla \underline{u}\right)^{\mathrm{e}}\right) \simeq \theta \;\left(\underline{e}'_2 \otimes \underline{e}'_1 - \underline{e}'_1 \otimes \underline{e}'_2\right) \tag{6}$$

In the infinitesimal deformation framework, the Nye's tensor $\underset{\sim}{\alpha}$ is introduced as a refined measure of lattice curvature, capturing the incompatibility inherent in the plastic distortion tensor, Eq. (7). This consideration is particularly useful for breaking the equivalence ratio between the slip and kink bands, since the kink bands are accompanied by the lattice rotation whereas slip bands are not. Further technical details about the Nye's tensor, including its derivation and additional properties, are provided in Appendix A.

$$\underset{\sim}{\alpha} = -\nabla \times \left(\nabla \underline{u}\right)^p \tag{7}$$

Considering the Nye's tensor as the internal variable, under static deformation, in the absence of body, and inertial forces, the principle of virtual power can be written for any subset of the lattice and its boundary:

$$\int_B \left(\underset{\sim}{\sigma} : \dot{\nabla} \underline{u}^{tot} + \underset{\sim}{s} : \left(\dot{\nabla} \underline{u}\right)^p + \underset{\sim}{M} : \nabla \times \left(\dot{\nabla} \underline{u}\right)^p\right) \, dV = \tag{8}$$

$$\int_{\partial B} \left(\underline{t}.\underline{u} + \underset{\sim}{m} : \left(\dot{\nabla} \underline{u}\right)^p\right) dS \qquad \forall \dot{\underline{u}},\ \forall \left(\dot{\nabla} \underline{u}\right)^p,\ \forall B \in \mathcal{B},\ \forall \partial B \in \partial \mathcal{B} \tag{9}$$

Here, $\underset{\sim}{s}$ and $\underset{\sim}{M}$ denote the micro-stress tensor and the double-stress tensor, which are respectively work-conjugate to $\left(\nabla \underline{u}\right)^p$ and $\nabla \times \left(\nabla \underline{u}\right)^p$. In addition, $\underline{t}$ represents the classical Cauchy traction vector, and $\underset{\sim}{m}$ is the corresponding double traction tensor. By applying classical variational arguments, the principle of virtual power leads to the following balance equations and boundary conditions:

$$\nabla \cdot \underset{\sim}{\sigma} = \underline{0}, \qquad \forall \underline{x} \in \mathcal{B}, \tag{10}$$

$$\underset{\sim}{s} + \nabla \times \underset{\sim}{M} = \underset{\sim}{0}, \quad \forall \underline{x} \in \mathcal{B}, \tag{11}$$

$$\underline{t} = \underset{\sim}{\sigma} \cdot \underline{n}, \qquad \forall \underline{x} \in \partial\mathcal{B}, \tag{12}$$

$$\underset{\sim}{m} = \underset{\sim}{M} \cdot \underset{\simeq}{\epsilon} \cdot \underline{n}, \qquad \forall \underline{x} \in \partial\mathcal{B}. \tag{13}$$

Here, $\underline{n}$ denotes the outward normal to the boundary surface. Following the consistent thermodynamic framework, the free energy is formulated in terms of the quadratic forms of the elastic strain $\underset{\sim}{\varepsilon}^e$, the curl of the plastic distortion tensor $\nabla \times \left(\nabla \underline{u}\right)^p$, and the cumulative shear strain γ^α_{cum}. Notably, the higher-order modulus is defined as a function of the cumulative shear strain associated with each slip system, $A = A\left(\gamma^\alpha_{cum}\right) = A^\alpha$.

$$\rho\psi = \rho\psi(\underset{\sim}{\varepsilon}^e, \nabla \times \left(\nabla \underline{u}\right)^p, \gamma^\alpha_{cum}, \gamma^\alpha) = \tfrac{1}{2}\underset{\sim}{\varepsilon}^e : \underset{\approx}{C} : \underset{\sim}{\varepsilon}^e + \tfrac{1}{2}A\left(\gamma^\alpha_{cum}\right)\nabla \times \left(\nabla \underline{u}\right)^p : \nabla \times \left(\nabla \underline{u}\right)^p + \rho\psi^h\left(\gamma^\alpha_{cum}\right) \tag{14}$$

Applying the Clausius–Duhem inequality leads[1]:

$$\begin{aligned} &\left[\underset{\sim}{\sigma} - \underset{\approx}{C} : \underset{\sim}{\varepsilon}^e\right] : \underset{\sim}{\dot{\varepsilon}}^e + \left[\underset{\sim}{\sigma} + \underset{\sim}{s}\right] : \left(\nabla \dot{\underline{u}}\right)^p - \tfrac{1}{2}\left[\nabla \times \left(\nabla \underline{u}\right)^p : \nabla \times \left(\nabla \underline{u}\right)^p\right] \frac{\partial A^\alpha}{\partial \gamma^\alpha}\dot{\gamma}^\alpha \\ &+ \left[\underset{\sim}{M}^\alpha - A^\alpha \nabla \times \left(\nabla \underline{u}\right)^p\right] : \nabla \times \left(\nabla \dot{\underline{u}}\right)^p - \rho\frac{\partial \psi^h}{\partial \gamma^\alpha_{cum}}\dot{\gamma}^\alpha_{cum} \geq 0 \end{aligned} \tag{15}$$

By assuming that the power associated with the elastic strain and the curl of the plastic distortion tensor are non-dissipative, two constitutive equations can be derived. These equations govern the Cauchy stress tensor (Eq. (16)) and the double-stress tensor (Eq. (17)).

$$\underset{\sim}{\sigma} = \underset{\approx}{C} : \underset{\sim}{\varepsilon}^e \tag{16}$$

$$\underset{\sim}{M}^\alpha = A^\alpha \nabla \times \left(\nabla \underline{u}\right)^p \tag{17}$$

By substituting Eq. (17) into the generalized balance equation, Eq. (11), and applying the relevant mathematical identities, the micro-stress can be expressed in terms of the higher-order modulus and the plastic distortion tensor.

$$\underset{\sim}{s}^\alpha = -\nabla \times \underset{\sim}{M}^\alpha = -\nabla \times \left(A^\alpha \nabla \times \left(\nabla \underline{u}\right)^p\right) = -\left[\{\nabla A^\alpha\} \times \nabla \times \left(\nabla \underline{u}\right)^p + A^\alpha\left\{\nabla \times \nabla \times \left(\nabla \underline{u}\right)^p\right\}\right] \tag{18}$$

$$= -\left(\nabla A^\alpha\right) \times \nabla \times \left(\nabla \underline{u}\right)^p - A^\alpha\left\{\nabla \otimes \nabla . \left(\nabla \underline{u}\right)^p - \Delta\left(\nabla \underline{u}\right)^p\right\} \tag{19}$$

The remaining terms in the Clausius–Duhem inequality are interpreted as dissipated powers during deformation, and are therefore attributed to the lattice's residual dissipation.

$$D^{\text{tot}} = \sum_\alpha D^\alpha = \sum_\alpha \left|\tau^\alpha - \chi^\alpha - \Gamma^\alpha\right| \dot{\gamma}^\alpha - \tau^\alpha_{cr}\dot{\gamma}^\alpha_{cum} \geq 0 \tag{20}$$

Here, τ^α represents the resolved shear stress, χ^α is the back-stress, and Γ^α is the generalized back-stress. The critical resolved shear stress for each slip system, $\tau^\alpha_{cr} = \rho d\psi^h/d\gamma^\alpha_{cum}$, is defined accordingly. The individual definitions of these variables are provided below.

$$\tau^\alpha = \underset{\sim}{\sigma}^\alpha : \underline{m}^\alpha \otimes \underline{n}^\alpha \tag{21}$$

$$\chi^\alpha = -\underset{\sim}{s}^\alpha : \underline{m}^\alpha \otimes \underline{n}^\alpha \tag{22}$$

$$\Gamma^\alpha = \tfrac{1}{2}\left[\nabla \times \left(\nabla \underline{u}\right)^p : \nabla \times \left(\nabla \underline{u}\right)^p\right] \frac{\partial A^\alpha}{\partial \gamma^\alpha} \tag{23}$$

Furthermore, the Schmid yield function is assumed by Eq. (24), accordingly the dissipation potential, $\Omega^\alpha\left(f^\alpha\right)$, is defined as a function of this yield function. In order to maintain the non-negativity of dissipation during deformation, and thus satisfy the Clausius–Duhem inequality, the dissipation potential must fulfill the condition $\frac{\partial \Omega^\alpha}{\partial f^\alpha} > 0$. Accordingly, the explicit form of the dissipation potential is given by Eq. (25), involving the Norton flow coefficient K, the Norton flow exponent n, and the Macaulay bracket.

$$f^\alpha = \left|\tau^\alpha - \chi^\alpha - \Gamma^\alpha\right| - \tau^\alpha_{cr} \tag{24}$$

$$\Omega^\alpha = \Omega^\alpha\left(f^\alpha\right) = \frac{K}{n+1}\left\langle \frac{\left|\tau^\alpha - \chi^\alpha - \Gamma^\alpha\right| - \tau^\alpha_{cr}}{K} \right\rangle^{n+1} \tag{25}$$

By enforcing the normality rule on the yield surface, the expressions for the shear strain rate, Eq. (26), and the cumulative shear strain rate associated with each slip system, Eq. (27), are derived.

$$\dot{\gamma}^\alpha = \frac{\partial \Omega^\alpha}{\partial f^\alpha}\text{sign}\left(\tau^\alpha - \chi^\alpha - \Gamma^\alpha\right) = \left\langle \frac{\left|\tau^\alpha - \chi^\alpha - \Gamma^\alpha\right| - \tau^\alpha_{cr}}{K} \right\rangle^n \text{sign}\left(\tau^\alpha - \chi^\alpha - \Gamma^\alpha\right) \tag{26}$$

$$\dot{\gamma}^\alpha_{cum} = \frac{\partial \Omega^\alpha}{\partial f^\alpha} = \left|\dot{\gamma}^\alpha\right| \tag{27}$$

---

[1] Due to the Eq. (27): $\frac{\partial A}{\partial \gamma^\alpha_{cum}}\dot{\gamma}^\alpha_{cum} = \frac{\partial A}{\partial \gamma^\alpha}\frac{\partial \gamma^\alpha}{\partial \gamma^\alpha_{cum}}\text{Sign}\left(\gamma^\alpha\right)\dot{\gamma}^\alpha = \frac{\partial A}{\partial \gamma^\alpha}\dot{\gamma}^\alpha$.

This study further investigates the formation of shear bands in irradiated microstructures, commonly known as clear channels (Mahajan and Eyre, 2017). These localized deformation pathways arise from the complex interplay between dislocation glide and irradiation-induced defects, such as Frank loops. For example, upon the onset of plastic deformation, dislocation glide is significantly accelerated. The mobile dislocations interact with and progressively eliminate irradiation-induced obstacles, effectively sweeping them away. This results in the creation of regions with diminished hardening defects, giving rise to localized softening zones within the microstructure. These softened regions exhibit elevated plastic deformation and reduced critical resolved shear stress, which are defining features of clear channels. To accurately represent this behavior, an exponential softening term dependent on the cumulative shear strain associated to each slip system, $\gamma^{\alpha}_{\mathrm{cum}}$, is incorporated into the critical resolved shear stress formulation (Lame Jouybari et al., 2024). This constitutive modification captures the essential mechanism whereby increased plastic strain leads to a progressive reduction in critical resolved shear stress, reflecting the annihilation of irradiation defects and the formation of clear channels.

$$\tau^{\alpha}_{\mathrm{cr}} = \rho \frac{d\psi^{h}}{d\gamma^{\alpha}_{cum}} = \tau^{\alpha}_{0} - \triangle\tau^{\alpha}\left[1 - \exp\left(-\frac{\gamma^{\alpha}_{cum}}{\gamma_0}\right)\right] \tag{28}$$

Here, τ^{α}_{0}, $\triangle\tau^{\alpha}$, and γ_0 respectively denote the initial critical resolved shear stress, the maximum softening, and the softening rate parameters.[2]

Previous experimental investigations involving microbending and microtorsion tests demonstrated that the material length scale parameter in strain gradient plasticity theories should not be treated as a constant (Stolken and Evans, 1998; Fleck et al., 1994). Instead, to accurately capture the experimentally observed stress–strain responses across different specimen geometries and loading modes, this parameter must evolve with deformation. These findings motivate the hypothesis adopted in this study: the material length scale, which governs the influence of strain gradients on mechanical strength and hardening behavior, is not an intrinsic material constant. Rather, it is intrinsically coupled to the evolving microstructural state during plastic deformation. In particular, for torsional loading of solid wires, it was observed that in order for the stress to remain finite at the wire center, the length scale must vary with the accumulated plastic strain. Supporting this view, (Gracio, 1994) proposed that the length scale decreases progressively with increasing plastic strain, eventually approaching a saturation value under large deformations. This behavior implies that the length scale parameter is more appropriately treated as a function of the accumulated plastic deformation, rather than as a fixed quantity. Building on this perspective, and considering the context of shear band formation in irradiated crystalline materials — where the critical resolved shear stress plays a pivotal role in describing the evolving microstructure — this study introduces a constitutive relation in which the higher-order modulus, A^{α}, is formulated as a function of the evolving critical resolved shear stress, $A^{\alpha} = g\left(\tau^{\alpha}_{\mathrm{cr}}\left(\gamma^{\alpha}_{\mathrm{cum}}\right)\right)$. This formulation captures the experimentally supported dependence of the higher-order mechanical response on both microstructural evolution and plastic strain accumulation.

Finally, the higher-order modulus A^{α} is defined as the second derivative of the hardening portion of the free energy, $\rho\psi^{h}$, with respect to the cumulative shear strain in each slip system.

$$A^{\alpha} := -\rho\left(\frac{\Lambda_0}{2\pi}\right)^{2}\frac{d^{2}\psi^{h}}{d\gamma^{\alpha 2}_{cum}} = -\left(\frac{\Lambda_0}{2\pi}\right)^{2}\frac{d\tau^{\alpha}_{\mathrm{cr}}}{d\gamma^{\alpha}_{cum}} = \left(\frac{\Lambda_0}{2\pi}\right)^{2}\frac{\triangle\tau^{\alpha}}{\gamma_0}\exp\left(-\frac{\gamma^{\alpha}_{cum}}{\gamma_0}\right) \tag{29}$$

Here, the microstructural characteristics associated with softening behavior, specifically, the maximum softening magnitude $\triangle\tau^{\alpha}$, the softening rate parameter γ_0, and the accumulated plastic deformation $\gamma^{\alpha}_{\mathrm{cum}}$, are incorporated into the constitutive definition of the higher-order modulus A^{α}. To maintain dimensional consistency within the generalized balance of microforces, as expressed in Eq. (11), a scaling factor of the form $\left(\Lambda_0/2\pi\right)^{2}$ is introduced. Here, Λ_0 is a material length parameter with units of meter, ensuring that the contribution of the softening-dependent higher-order term is physically meaningful and compatible with the governing equations. This definition of the higher-order modulus plays a crucial role in linking the effects of strain gradient theory to the softening mechanism induced by irradiation and, consequently, to the formation of shear bands.[3] Furthermore, to compare the higher-order modulus in the Enhanced-SGCP theory with the length scale in the Classical-SGCP theory:

$$\gamma^{\alpha}_{cum} = 0 \quad : \quad A^{\alpha} = \left(\frac{\Lambda_0}{2\pi}\right)^{2}\frac{\triangle\tau^{\alpha}}{\gamma_0} = A \tag{30}$$

2.2. Classical-SGCP: Constant length scale during deformation

In the classical strain gradient crystal plasticity theory (Marano et al., 2021), the curl of the plastic distortion tensor is established as the internal variable for the strain gradient theory. By applying the principle of virtual power under this assumption, the same classical and generalized balance Eqs. ((10), (11)), along with the corresponding classical and generalized traction tensors Eqs. ((12), (13)), are derived as in the Enhanced-SGCP theory. However, in this classical formulation, the length scale is treated as a constant parameter in the free energy, implying $A = \mathrm{Const.}$

$$\rho\psi = \rho\psi(\underset{\sim}{\varepsilon}^{e}, \nabla\times\left(\nabla\underline{u}\right)^{p}, \gamma^{\alpha}_{cum}, \gamma^{\alpha}) = \tfrac{1}{2}\underset{\sim}{\varepsilon}^{e} : \underset{\approx}{C} : \underset{\sim}{\varepsilon}^{e} + \tfrac{1}{2}A\nabla\times\left(\nabla\underline{u}\right)^{p} : \nabla\times\left(\nabla\underline{u}\right)^{p} + \rho\psi^{h}\left(\gamma^{\alpha}_{cum}\right) \tag{31}$$

---

[2] These material parameters are correlated with the experimental physics-based models of the irradiated crystal (Lame Jouybari et al., 2024).

[3] It is worth noting that various expressions for the higher-order modulus as a function of critical resolved shear stress have been investigated (not shown here). Among them, the physically meaningful length scale that correlates directly with the width of the observed shear bands is the current formulation of the higher order modulus.

By applying the Clausius–Duhem inequality, the length scale no longer has a time derivative, and as a result, the generalized back-stress vanishes ($\Gamma^\alpha = 0$).

$$\left[\underset{\sim}{\sigma} - \underset{\approx}{\Lambda} : \underset{\sim}{\varepsilon}^{e}\right] : \dot{\underset{\sim}{\varepsilon}}^{e} + \left[\underset{\sim}{\sigma} + \underset{\sim}{s}\right] : \left(\nabla\dot{\underline{u}}\right)^{p} + \left[\underset{\sim}{M} - A\nabla\times\left(\nabla\underline{u}\right)^{p}\right] : \nabla\times\left(\nabla\dot{\underline{u}}\right)^{p} - \rho\frac{\partial\psi^{h}}{\partial\gamma^{\alpha}_{cum}}\dot{\gamma}^{\alpha}_{cum} \geq 0 \tag{32}$$

Under the same assumptions as in the Enhanced-SGCP theory, namely that the power associated with the elastic strain and the curl of the plastic distortion tensor are non-dissipative, the same expressions for the Cauchy stress tensor, Eq. (16), and the double-stress tensor, Eq. (17), are obtained. However, by substituting Eq. (17) into the generalized balance equation, Eq. (11), the resulting micro-stress tensor differs from that in the Enhanced-SGCP theory, Eq. (19), because the gradient of the length scale vanishes, $\nabla A = \underline{0}$.

$$\underset{\sim}{s} = -\nabla\times\left(\underset{\sim}{M}\right) = -\nabla\times\left(A\nabla\times\left(\nabla\underline{u}\right)^{p}\right) = -A\left\{\nabla\times\nabla\times\left(\nabla\underline{u}\right)^{p}\right\} = -A\left\{\nabla\otimes\nabla.\left(\nabla\underline{u}\right)^{p} - \Delta\left(\nabla\underline{u}\right)^{p}\right\} \tag{33}$$

Additionally, by assigning the dissipative powers to the lattice's residual dissipation, Eq. (34), and adopting the Schmid yield function $f^\alpha = |\tau^\alpha - \chi^\alpha| - \tau^\alpha_{cr}$, along with the corresponding dissipation potential, Eq. (35), the evolution of the shear strain rate is derived by Eq. (36).

$$D^{\text{tot}} = \sum_{\alpha} D^{\alpha} = \sum_{\alpha} |\tau^{\alpha} - \chi^{\alpha}|\,\dot{\gamma}^{\alpha} - \tau^{\alpha}_{cr}\dot{\gamma}^{\alpha}_{cum} \geq 0 \tag{34}$$

$$\Omega^{\alpha} = \Omega^{\alpha}\left(f^{\alpha}\right) = \frac{K}{n+1}\left\langle\frac{|\tau^{\alpha} - \chi^{\alpha}| - \tau^{\alpha}_{cr}}{K}\right\rangle^{n+1} \tag{35}$$

$$\dot{\gamma}^{\alpha} = \left\langle\frac{|\tau^{\alpha} - \chi^{\alpha}| - \tau^{\alpha}_{cr}}{K}\right\rangle^{n}\operatorname{sign}\left(\tau^{\alpha} - \chi^{\alpha}\right) \tag{36}$$

2.3. Higher-order interface condition on grain boundary

Both the Classical[4] and Enhanced-SGCP theories introduce the generalized traction tensor, as defined in Eq. (13), based on the principle of virtual power. In this study, three types of higher-order interface conditions on grain boundaries are examined,[5] each defined using the generalized traction vector in polycrystalline simulations. The conditions such as MicroFree, MicroContinuity, and MicroHard, represent varying levels of resistance offered by the grain boundary to dislocation transmission between grains. The MicroFree condition assumes that the grain boundary provides no resistance to dislocation glide. Under this condition, dislocations reaching the grain boundary transmit freely to the adjacent grain. Consequently, both the back-stress, χ^α, and the generalized back-stress, Γ^α, vanish at the grain boundary. Computationally, this is achieved by setting $A^\alpha = 0$ at the grain boundary. The MicroContinuity condition represents an intermediate scenario in which the generalized traction tensor, $\underset{\sim}{m}$, is continuous across the grain boundary. This implies that both the back-stress, χ^α, and the generalized back-stress, Γ^α, are also continuous at the grain boundary, ensuring a smoother transition of stresses. The MicroHard condition is the most restrictive, assuming that the grain boundary completely blocks dislocation transmission between grains. This condition results in significantly high values of back-stress, χ^α, and generalized back-stress, Γ^α, at the grain boundary. Computationally, this is implemented by assigning $\tau^\alpha = 10^5\tau_0$ at the grain boundary, effectively halting the shear strain rate, as described by Eq. (26).

These higher-order interface conditions provide a nuanced framework for understanding and modeling the behavior of grain boundaries in polycrystalline materials under varying levels of mechanical resistance.

2.4. FFT method

The FFT method was initially introduced and applied to the homogenization of composites with nonlinear behavior (Moulinec and Suquet, 1998). Today, it is recognized as a valuable computational alternative to the finite element method (FEM), offering distinct advantages and limitations. One of the primary benefits of the FFT method is its lower computational cost, scaling as $O(N\log(N))$ compared to $O\left(N^2\right)$ complexity of FEM. This efficiency is particularly advantageous for simulations requiring high resolution. Additionally, the FFT method significantly reduces memory allocation requirements and allows the direct use of EBSD images of microstructures without the need for meshing or selecting element types. The inherent periodicity of fields in FFT-based computations further simplifies analyses, whereas FEM often requires additional computational resources to enforce periodic boundary conditions. These advantages have led to the widespread adoption of the FFT method across various fields of continuum solid mechanics. Over the years, several categories of FFT algorithms have been proposed to address different applications and challenges. Examples include fixed-point iteration schemes in SGCP theory (Lame Jouybari et al., 2024; Marano et al., 2021), the polarization approach (Wicht et al., 2021), the Fourier–Galerkin scheme (Lucarini and Segurado, 2019), and displacement-based FFT approach (Lucarini et al., 2021). As a result, the FFT method has evolved into a robust and versatile tool for computational mechanics.

---

[4] In this model, only the back-stress is applicable for the following statements.

[5] Other types of internal boundaries, such as phase boundaries, twin boundaries, dislocation walls, subgrain boundaries, crack tips, and voids, can be accommodated by the proposed theoretical framework.

In this study, the fixed-point iteration method is employed to solve the governing constitutive equations derived from the Enhanced-SGCP theory, as represented in Eqs. (10) and (11). The fixed-point FFT algorithm consists of three main components: (I) Initialization at Zeroth FFT Iteration, (II) FFT Iteration for solving the *Lippmann–Schwinger* equation (equivalent to the classical balance equation), and (III) Solving the generalized balance equation. Significant advancements in the first two parts of the FFT algorithm were achieved in previous work (Lame Jouybari et al., 2024), including the implementation of the rotated scheme Green operator (Willot, 2015), an arc-length method for mixed boundary conditions under tensile loading (Michel et al., 1999), and a 21-voxel finite difference scheme (Neumann et al., 2002) for solving the generalized balance equation according to the strict microslip Classical-SGCP model. Furthermore, an alternate $2-\delta$ type of Anderson acceleration (Ramière and Helfer, 2015) was also incorporated. Consequently, the first two parts of the FFT algorithm proposed in this study, outlined in Table 1 (Steps 1–10), remain consistent with the approach detailed in (Lame Jouybari et al., 2024). For a comprehensive discussion on these components, readers are referred to the previous work. The focus of this study lies in the third part of the FFT algorithm, which differs from the earlier work. To briefly recall the first two parts, the so-called "local problem" is formulated in nonhomogeneous elastic material (Moulinec and Suquet, 1998). The formulation begins with a additive decomposition of the total displacement gradient tensor field into average and fluctuation parts. It is assumed that the fluctuation term of the displacement gradient tensor field exhibits periodic behavior, while the classical Cauchy traction remains non-periodic. A reference isotropic linear elastic material, characterized by the elasticity tensor $\underset{\approx}{C}^0$, is introduced. Based on this, a polarization tensor field ($\underset{\sim}{\tau}$) is defined. By considering the classical balance equation, Eq. (10), and the constitutive equation for the Cauchy stress tensor, Eq. (16), the solution is iteratively obtained using the *Lippmann–Schwinger* equation (Lippmann and Schwinger, 1950) in both real and Fourier space.

$$\begin{cases} \nabla \underline{u}(\underline{x}) = \overline{\nabla \underline{u}} + \nabla \underline{u}^{\star}(\underline{x}) & \forall\, \underline{x} \in \mathcal{B}, \quad \nabla \underline{u}^{\star}\#\partial\mathcal{B} \\ \underset{\sim}{\sigma}(\underline{x}) = \underset{\approx}{C}(\underline{x}) : \nabla \underline{u}(\underline{x}) & \forall\, \underline{x} \in \mathcal{B}, \quad \underset{\sim}{\sigma}.\underline{n} - \#\partial\mathcal{B} \\ \underset{\sim}{\tau}(\underline{x}) = \underset{\sim}{\sigma}(\underline{x}) - \underset{\approx}{C}^0 : \nabla \underline{u}(\underline{x}) & \forall\, \underline{x} \in \mathcal{B} \\ \nabla \cdot \underset{\sim}{\sigma}(\underline{x}) = \underline{0} & \forall\, \underline{x} \in \mathcal{B} \end{cases} \tag{37}$$

Accordingly, the total displacement gradient tensor field, as the solution to the *Lippmann–Schwinger* equation, can be determined using two equivalent approaches. In real space, it is expressed as a convolution between the Green operator ($\underset{\approx}{\mathrm{G}}$) and the polarization tensor, as shown in Eq. (38). Alternatively, in Fourier space, it is represented by a double contraction between the Green operator[6] and the polarization tensor, as described in Eq. (39). The second approach in Fourier space provides a consistent framework for solving the displacement gradient tensor field, leveraging the computational efficiency of Fourier transformations to handle periodic boundary conditions effectively.

$$\text{Real space:} \qquad \nabla \underline{u}^{\mathrm{tot}}(\underline{x}) = \overline{\nabla \underline{u}} - \underset{\approx}{\mathrm{G}} * \underset{\sim}{\tau}(\underline{x}) \tag{38}$$

$$\text{Fourier space:} \qquad \begin{cases} \widehat{\nabla \underline{u}}^{\mathrm{tot}}(\underline{\xi}) = -\underset{\approx}{\widehat{\mathrm{G}}}(\underline{\xi}) : \underset{\sim}{\hat{\tau}}(\underline{\xi}) & \forall\, \underline{\xi} \neq \underline{0}, \\ \widehat{\nabla \underline{u}}^{\mathrm{tot}}(\underline{0}) = \overline{\nabla \underline{u}} & \underline{\xi} = \underline{0}. \end{cases} \tag{39}$$

Upon obtaining the converged displacement gradient tensor field from the first two stages of the FFT algorithm, the cumulative shear strain associated with each slip system (γ^{α}_{cum}) and the plastic distortion tensor ($\nabla \underline{u}^p$) are utilized as inputs for the third stage of the FFT algorithm, which specifically addresses the Enhanced-SGCP theory. This stage focuses on solving the generalized balance equation to account for higher-order effects. The process begins with the evaluation of the higher-order modulus (A^{α}) in Table 1, Step 11, derived using Eq. (29). Subsequently, in Step 12, the plastic distortion tensor is transformed into Fourier space to facilitate the efficient computation of differential operators. In Step 13(a), the curl of the plastic distortion tensor is calculated by applying the frequency-domain representation of the curl operator to the Fourier-transformed plastic distortion tensor. This result is then transformed back into real space using the inverse Fourier transform. Similar operations are carried out in Steps 13(b-d) to evaluate the gradient of the higher-order modulus, the gradient-divergence of the plastic distortion tensor, and the Laplacian of the plastic distortion tensor, respectively. Additional details on these computations are provided in Appendix C. With these terms computed, the micro-stress associated with each slip system is determined in Step 14 of Table 1 using Eq. (19). Subsequently, the back-stress contributions for each slip system are evaluated in Step 15. Finally, the generalized back-stress is calculated based on Eq. (23) in Step 16. This systematic approach ensures the accurate and consistent implementation of the Enhanced-SGCP theory.

The FFT algorithm for the Classical-SGCP model, as outlined in Table 2, begins by transforming the plastic distortion tensor into Fourier space at Step 11. Following this, in Step 12(a) and 12(b), the gradient-divergence and Laplacian operators of the plastic distortion tensor are computed, leveraging the efficiency of Fourier-based operations. Subsequently, at Step 12(c), the micro-stress tensor is evaluated based on the derived quantities. Finally, at Step 14, the back-stress associated with each slip system is calculated, completing the essential steps of the algorithm in the Classical-SGCP model.

3. Results

3.1. Analytical solution of the enhanced SGCP model

In this section, a two-dimensional single crystal with a single slip system is considered to introduce idealized slip and kink bands. The generalized tensors and state variables associated with the Enhanced-SGCP framework are subsequently derived in their tensor

---

[6] $\underline{\xi}$ denotes the frequency in the Fourier space.

Table 1
Pseudocode for the FFT method implementation in the Enhanced-SGCP theory.

```
Initialization at Zeroth Iteration: $i = 0$
1. Extrapolate the displacement gradient tensor to the new time step:
   $\nabla\underline{u}^i(t_n + \Delta t_n) = \nabla\underline{u}(t_n) + \frac{\Delta t_n}{\Delta t_{n-1}}\left[\nabla\underline{u}(t_n) - \nabla\underline{u}(t_{n-1})\right]$
2. Perform implicit time integration of state variables: (see Appendix D)
   $\left\{(\nabla\underline{u})^e\left(t_n + \Delta t\right), \gamma^\alpha\left(t_n + \Delta t\right), (\nabla\underline{u})^p\left(t_n + \Delta t\right), \underset{\sim}{\sigma}\left(t_n + \Delta t\right), \tau^\alpha\left(t_n + \Delta t\right), \tau^\alpha_{cr}\left(t_n + \Delta t\right)\right\}$

FFT Iteration: $i = i + 1$
3. Test for convergence of the linear momentum balance equation (see (Lame Jouybari et al., 2024)).
4. Compute the polarization tensor field:
   4.1 Evaluate in real space:
       $\underset{\sim}{\tau}^i(\underline{x}) = \underset{\sim}{\sigma}^i(\underline{x}) - \underset{\approx}{C}^0 : \nabla\underline{u}^i(\underline{x})$
   4.2 Transform to Fourier space:
       $\underset{\sim}{\hat{\tau}}^i(\underline{\xi}) = \mathcal{FFT}\left(\underset{\sim}{\tau}^i\right)$
5. Apply mixed boundary conditions for tensile loading (see (Michel et al., 1999)).
6. Update the displacement gradient tensor:
   6.1 Compute in Fourier space for the new iteration:
       $\widehat{\nabla\underline{u}}^{i+1}(\underline{\xi}) = -\underset{\approx}{\hat{\mathrm{G}}}(\underline{\xi}) : \underset{\sim}{\hat{\tau}}^i(\underline{\xi}) \quad \forall\underline{\xi} \neq \underline{0}$
       $\widehat{\nabla\underline{u}}^{i+1}(\underline{0}) = \overline{\nabla\underline{u}}^i \qquad \underline{\xi} = \underline{0}$
   6.2 Perform the inverse transform to real space:
       $\nabla\underline{u}^{i+1}(\underline{x}) = \mathcal{IFFT}\left(\widehat{\nabla\underline{u}}^{i+1}(\underline{\xi})\right)$
7. Apply Anderson acceleration every three iterations (see (Lame Jouybari et al., 2024)).
8. Perform implicit time integration of state variables: (see Appendix D)
   $\left\{(\nabla\underline{u})^e\left(t_n + \Delta t\right), \gamma^\alpha\left(t_n + \Delta t\right), (\nabla\underline{u})^p\left(t_n + \Delta t\right), \underset{\sim}{\sigma}\left(t_n + \Delta t\right), \tau^\alpha\left(t_n + \Delta t\right), \tau^\alpha_{cr}\left(t_n + \Delta t\right)\right\}$
9. Test for convergence under mixed boundary conditions (see (Lame Jouybari et al., 2024)).
10. If all convergence criteria are satisfied, proceed to step 11; otherwise, return to step 3.

Generalized Balance Equation
11. Evaluate the higher-order modulus:
    $A^\alpha = \left(\frac{\Lambda_0}{2\pi}\right)^2 \frac{\Delta\tau^\alpha}{\gamma_0} \exp\left(-\frac{\gamma^\alpha_{cum}}{\gamma_0}\right).$
12. Transform the plastic distortion tensor to Fourier space:
    $\widehat{(\nabla\underline{u})^p} = \mathcal{FFT}\left((\nabla\underline{u})^p\right).$
13. Compute auxiliary terms:
    a. Curl of the plastic distortion tensor:
       $\nabla \times (\nabla\underline{u})^p = \mathcal{IFFT}\left(\widehat{\mathrm{Curl}}\,\widehat{(\nabla\underline{u})^p}\right).$
    b. Gradient of the higher-order modulus:
       $\nabla A^\alpha = \mathcal{IFFT}\left(\widehat{\mathrm{Grad}}\,\hat{A}\right).$
    c. Gradient-divergence of the plastic distortion tensor:
       $\nabla \otimes \nabla.\,(\nabla\underline{u})^p = \mathcal{IFFT}\left(\widehat{\mathrm{Grad\text{-}Div}}\,\widehat{(\nabla\underline{u})^p}\right).$
    d. Laplacian of the plastic distortion tensor:
       $\Delta\,(\nabla\underline{u})^p = \mathcal{IFFT}\left(\widehat{\mathrm{Lap}}\,\widehat{(\nabla\underline{u})^p}\right).$
14. Evaluate the micro-stress tensor:
    $\underset{\sim}{s}^\alpha = -(\nabla A^\alpha) \times \left(\nabla \times (\nabla\underline{u})^p\right) - A^\alpha \nabla \otimes \nabla.\,(\nabla\underline{u})^p + A^\alpha \Delta\,(\nabla\underline{u})^p.$
15. Compute the back-stress:
    $\chi^\alpha = -\underset{\sim}{s}^\alpha : \left(\underline{m}^\alpha \otimes \underline{n}^\alpha\right).$
16. Evaluate the generalized back-stress:
    a. Derivative of the higher-order modulus:
       $\frac{\partial A^\alpha}{\partial\gamma^\alpha} = -\frac{A^\alpha}{\gamma_0}\,\mathrm{Sign}(\gamma^\alpha).$
    b. Evaluate the generalized back-stress:
       $\Gamma^\alpha = \frac{1}{2}\left[\nabla \times (\nabla\underline{u})^p : \nabla \times (\nabla\underline{u})^p\right] \frac{\partial A^\alpha}{\partial\gamma^\alpha}.$
17. Update the time step.
```

component form. Finally, the differential equation corresponding to the generalized balance equation is formulated and solved analytically.

3.1.1. Slip band

Consider a two-dimensional single crystal of infinite length along the $\underline{e}_1$ direction, with its boundaries in the $\underline{e}_2$ direction embedded in pure elastic layers, Fig. 1(a). The slip system of the crystal is characterized by the slip direction and the normal to the slip plane, defined as $(\underline{e}_1, \underline{e}_2)$, respectively. The crystal is subjected to simple shear loading, and it is assumed that the distribution of variables remains homogeneous along the $\underline{e}_1$ and $\underline{e}_3$ coordinate directions. Under these assumptions, the displacement gradient tensor and the associated classical variables are explicitly expressed in terms of their tensor components.

$$\underline{u} = u(x_2)\underline{e}_1 \tag{40}$$

Table 2
Pseudocode for the FFT method implementation in the Classical-SGCP model.

```
Steps for the Generalized Balance Equation Solution
11. Transform the plastic distortion tensor into Fourier space:
    $\widehat{(\nabla \underline{u})^p} = \mathcal{FFT}\left((\nabla \underline{u})^p\right)$
12. Compute Micro-Stress:
    a. Compute the gradient-divergence of the plastic distortion tensor:
       $\nabla \otimes \nabla . (\nabla \underline{u})^p = \mathcal{IFFT}\left(\widehat{\text{Grad-Div}}\,\widehat{(\nabla \underline{u})^p}\right)$
    b. Compute the Laplacian of the plastic distortion tensor:
       $\Delta (\nabla \underline{u})^p = \mathcal{IFFT}\left(\widehat{\text{Lap}}\,\widehat{(\nabla \underline{u})^p}\right)$
    c. Evaluate the micro-stress tensor:
       $\underset{\sim}{s} = -A\,\nabla \otimes \nabla . (\nabla \underline{u})^p + A\,\Delta (\nabla \underline{u})^p$
13. Compute the Back-Stress:
    $\chi^\alpha = -\underset{\sim}{s} : (\underline{m}^\alpha \otimes \underline{n}^\alpha)$
14. Update the Time Step.
```

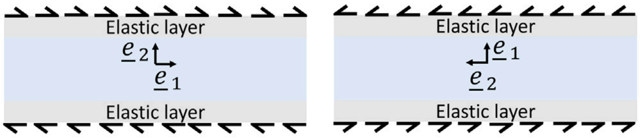

(a) Ideal slip band (b) Ideal kink band

Fig. 1. Schematic representation of ideal slip and kink bands under shear loading. The central region exhibits elasto-plastic behavior, embedded by two elastic layers.

$$\nabla \underline{u} = \frac{du}{dx_2} \underline{e}_1 \otimes \underline{e}_2 \tag{41}$$

$$\left(\nabla \underline{u}\right)^p = \gamma \underline{e}_1 \otimes \underline{e}_2 \tag{42}$$

$$\left(\nabla \underline{u}\right)^e = \frac{du}{dx_2} \underline{e}_1 \otimes \underline{e}_2 - \gamma \underline{e}_1 \otimes \underline{e}_2 \tag{43}$$

$$\underset{\sim}{\sigma} = 2\mu \left[\frac{du}{dx_2} - \gamma\right] \text{Sym}\left(\underline{e}_1 \otimes \underline{e}_2\right) \tag{44}$$

Accordingly, the generalized tensors derived from the Enhanced-SGCP framework are expressed explicitly in terms of their tensor components, as presented in the following equations.

$$\nabla \times \left(\left(\nabla \underline{u}\right)^p\right) = \frac{d\gamma}{dx_3} \underline{e}_1 \otimes \underline{e}_1 - \frac{d\gamma}{dx_1} \underline{e}_1 \otimes \underline{e}_3 = \underset{\sim}{0} \tag{45}$$

$$A = \left(\frac{\Lambda_0}{2\pi}\right)^2 \left(\frac{\Delta\tau}{\gamma_0}\right) \exp\left(-\frac{|\gamma|}{\gamma_0}\right) \tag{46}$$

$$\nabla A = A \left[\frac{-1}{\gamma_0} \frac{d|\gamma|}{dx_2}\right] \underline{e}_2 \tag{47}$$

$$\nabla \times \nabla \times \left(\left(\nabla \underline{u}\right)^p\right) = \underset{\sim}{0} \tag{48}$$

$$\underset{\sim}{s} = 0 \tag{49}$$

$$\chi = 0 \tag{50}$$

$$\nabla \times \left(\nabla \underline{u}\right)^p : \nabla \times \left(\nabla \underline{u}\right)^p = 0 \tag{51}$$

$$\Gamma^\alpha = 0 \tag{52}$$

Since the back-stress ($\chi = 0$) and the generalized back-stress ($\Gamma = 0$) are both zero, the Enhanced-SGCP model remains inactive within the slip band. Consequently, the results revert to those predicted by the CCP framework. According to (Asaro and Rice, 1977), plastic localization occurs due to the local softening behavior, leading to the formation of an ideal slip band. However, within the CCP framework, the width of this slip band remains undefined, as the CCP framework does not inherently account for any physical mechanisms that regulate its width. This limitation underscores the fact that the Nye tensor precisely accounts for the lattice rotation angle and curvature, both of which are zero within the slip band. Further details regarding the correlation between the Nye tensor and the lattice rotation angle are discussed in Appendix B.

3.1.2. Kink band

Unlike the infinite length along the $\underline{e}_1$ direction described in the ideal slip band, consider a two-dimensional single crystal that is infinite along the $\underline{e}_2$ direction, with elastic layers embedded at each boundary of the $\underline{e}_1$ direction, Fig. 1(b). In this scenario, the slip system of the crystal is also defined by the slip direction and the normal to the slip plane, represented as $(\underline{e}_1, \underline{e}_2)$, respectively. Similarly subjected to simple shear loading, it is now assumed that the distribution of variables remains homogeneous along the $\underline{e}_2$ and $\underline{e}_3$ coordinate directions. Under these assumptions, the displacement gradient tensor and associated classical variables are explicitly formulated in terms of their tensor components.

$$\underline{u} = u(x_1)\underline{e}_2 \tag{53}$$

$$\nabla\underline{u} = \frac{du}{dx_1}\underline{e}_2 \otimes \underline{e}_1 \tag{54}$$

$$\left(\nabla\underline{u}\right)^p = \gamma\underline{e}_1 \otimes \underline{e}_2 \tag{55}$$

$$\left(\nabla\underline{u}\right)^e = \frac{du}{dx_1}\underline{e}_2 \otimes \underline{e}_1 - \gamma\underline{e}_1 \otimes \underline{e}_2 \tag{56}$$

$$\underset{\sim}{\sigma} = 2\mu\left[\frac{du}{dx_1} - \gamma\right]\mathrm{Sym}\left(\underline{e}_1 \otimes \underline{e}_2\right) \tag{57}$$

Analogous to the ideal slip band, the generalized tensors within the Enhanced-SGCP framework according to this ideal kink band are explicitly formulated in terms of their tensor components.

$$\nabla \times \left(\left(\nabla\underline{u}\right)^p\right) = -\frac{d\gamma}{dx_1}\underline{e}_1 \otimes \underline{e}_3 \tag{58}$$

$$A = \left(\frac{\Lambda_0}{2\pi}\right)^2\left(\frac{\Delta\tau}{\gamma_0}\right)\exp\left(-\frac{|\gamma|}{\gamma_0}\right) \tag{59}$$

$$\nabla A = A\left[\frac{-1}{\gamma_0}\frac{d|\gamma|}{dx_1}\right]\underline{e}_1 \tag{60}$$

$$\nabla A \times \nabla \times \left(\left(\nabla\underline{u}\right)^p\right) = 0 \tag{61}$$

$$\nabla \times \nabla \times \left(\left(\nabla\underline{u}\right)^p\right) = -\frac{d^2\gamma}{dx_1^2}\underline{e}_1 \otimes \underline{e}_2 \tag{62}$$

$$\underset{\sim}{s} = A\frac{d^2\gamma}{dx_1^2}\underline{e}_1 \otimes \underline{e}_2 \tag{63}$$

$$\chi = -A\frac{d^2\gamma}{dx_1^2} \tag{64}$$

$$\nabla \times \left(\nabla\underline{u}\right)^p : \nabla \times \left(\nabla\underline{u}\right)^p = \left(\frac{d\gamma}{dx_1}\right)^2 \tag{65}$$

$$\frac{\partial A}{\partial\gamma} = \frac{-A}{\gamma_0}\mathrm{sign}\left(\gamma\right) \tag{66}$$

$$\Gamma = \frac{-A}{2\gamma_0}\left(\frac{d\gamma}{dx_1}\right)^2\mathrm{sign}\left(\gamma\right) \tag{67}$$

At the initial stage of plastic deformation, it is assumed here that the contributions from quadratic powered gradients are negligible, $\left(\frac{d\gamma}{dx_1}\right)^2 \approx 0$, and the resolved shear stress is higher than the back-stress ($\tau > \chi$). Consequently, for the ideal kink band, the Schmidt yield function is simplified and expressed in the following form.

$$f = \tau + \left(\frac{\Lambda_0}{2\pi}\right)^2\left(\frac{\Delta\tau}{\gamma_0}\right)\exp\left(-\frac{|\gamma|}{\gamma_0}\right)\frac{d^2\gamma}{dx_1^2} - \tau_0 + \Delta\tau\left[1 - \exp\left(-\frac{|\gamma|}{\gamma_0}\right)\right] \tag{68}$$

3.1.3. Analytical solution of kink band

During plastic deformation in an elasto-plastic crystal, the material behavior must remain constrained on the yield surface. To enforce this condition, the Schmidt yield function, given by Eq. (68), is set to zero throughout the plastic flow. This constraint leads to the following differential equation.[7]

$$\tau + \left(\frac{\Lambda_0}{2\pi}\right)^2\left(\frac{\Delta\tau}{\gamma_0}\right)\exp\left(-\frac{\gamma}{\gamma_0}\right)\frac{d^2\gamma}{dx^2} - \tau_0 + \Delta\tau\left[1 - \exp\left(-\frac{\gamma}{\gamma_0}\right)\right] = 0 \tag{69}$$

A new variable, defined in terms of the shear strain as $\Upsilon = \exp\left(-\frac{\gamma}{\gamma_0}\right)$, is introduced. The first and second derivatives of this variable are derived under the assumption that the quadratic term is negligible at the onset of plastic deformation.

$$\frac{d\Upsilon}{dx} = -\frac{1}{\gamma_0}\exp\left(-\frac{\gamma}{\gamma_0}\right)\frac{d\gamma}{dx} \tag{70}$$

---

[7] Since the crystal undergoes single slip, the superscript α is omitted in this section. Additionally, due to the nature of the loading and slip system, $\gamma_{cum} = \left|\gamma\right| = \gamma$. For simplicity in the notation, $x_1 = x$ is considered.

$$\frac{d^2Y}{dx^2} = -\frac{1}{\gamma_0}\exp\left(-\frac{\gamma}{\gamma_0}\right)\frac{d^2\gamma}{dx^2} + \frac{1}{\gamma_0^2}\exp\left(-\frac{\gamma}{\gamma_0}\right)\left(\frac{d\gamma}{dx}\right)^2 \simeq -\frac{1}{\gamma_0}\exp\left(-\frac{\gamma}{\gamma_0}\right)\frac{d^2\gamma}{dx^2} \tag{71}$$

By substituting the newly defined variable, $Y = \exp\left(-\frac{\gamma}{\gamma_0}\right)$, and Eq. (71) into the differential equation given by Eq. (69), the resulting equation simplifies to the following form.

$$\frac{d^2Y}{dx^2} + \left(\frac{2\pi}{\Lambda_0}\right)^2 Y = \left(\frac{2\pi}{\Lambda_0}\right)^2 \frac{\tau - \tau_0 + \Delta\tau}{\Delta\tau} \tag{72}$$

The solution to this differential equation can be expressed in terms of sine and cosine functions.

$$Y(x) = \alpha\cos\left(\frac{2\pi x}{\Lambda_0}\right) + \beta\sin\left(\frac{2\pi x}{\Lambda_0}\right) + \frac{\tau - \tau_0 + \Delta\tau}{\Delta\tau} \tag{73}$$

Due to the symmetry of the shear strain field distribution, it follows that $\beta = 0$. Furthermore, assuming that the shear strain is zero outside the kink band, which has a width of λ, and considering the continuity of the shear strain and the normal component of the double-stress tensor at the localization boundary, the following two boundary conditions are obtained for the kink band of width λ.

$$\begin{cases}\gamma_{cum}\left(\pm\frac{\lambda}{2}\right) = 0\\ \underset{\sim}{m}\left(\pm\frac{\lambda}{2}\right) = \underset{\sim}{0}\end{cases} \Rightarrow \begin{cases}Y\left(\pm\frac{\lambda}{2}\right) = 1\\ \frac{dY}{dx}\left(\pm\frac{\lambda}{2}\right) = 0\end{cases} \Rightarrow \begin{cases}\alpha = \frac{\tau-\tau_0}{\Delta\tau}\\ \lambda = \Lambda_0\end{cases} \tag{74}$$

It follows that the width of the kink band is precisely equal to the length scale in the higher-order modulus, Eq. (29), i.e., $\lambda = \Lambda_0$. Additionally, the shear strain distribution can be determined using the new variable Y.

$$\gamma = -\gamma_0 \ln\left[Y(x)\right] = -\gamma_0 \ln\left[\frac{\tau-\tau_0}{\Delta\tau}\cos\left(\frac{2\pi x}{\Lambda_0}\right) + \frac{\tau-\tau_0+\Delta\tau}{\Delta\tau}\right] \tag{75}$$

The only remaining variable to determine is the resolved shear stress, τ, which can be obtained by subtracting the shear strain from the total imposed shear loading.

$$\tau = \underset{\sim}{\sigma} : \underline{e}_1 \otimes \underline{e}_2 = \sigma_{12} = 2\mu\varepsilon^e_{12} = \mu\left[\overline{\gamma} - \frac{1}{L}\int_{-\frac{\lambda}{2}}^{\frac{\lambda}{2}} \gamma(x)\ dx\right] = \mu\left[\overline{\gamma} + \frac{\gamma_0}{L}\int_{-\frac{\lambda}{2}}^{\frac{\lambda}{2}} \ln\left[\alpha\cos\left(\frac{2\pi x}{\Lambda_0}\right) + \alpha + 1\right]\ dx\right] \tag{76}$$

Here L is the finite length of the single crystal. Furthermore, to evaluate the integral in Eq. (76), the following procedure is applied. Assuming that $\alpha < 1/2$, which can be satisfied by selecting appropriate material parameters for τ_0 and $\Delta\tau$, the natural logarithm inside the integral is accordingly replaced by its Taylor series expansion.

$$\ln\left[\alpha\cos\left(\frac{2\pi x}{\Lambda_0}\right) + \alpha + 1\right] \simeq \left[\alpha\cos\left(\frac{2\pi x}{\Lambda_0}\right) + \alpha\right] - \frac{1}{2}\left[\alpha\cos\left(\frac{2\pi x}{\Lambda_0}\right) + \alpha\right]^2 + \text{Higher Order Terms.} \tag{77}$$

The approximate expression for the integral in Eq. (77) can be obtained by noting that $(\int_{-\frac{\lambda}{2}}^{\frac{\lambda}{2}} \cos\left(\frac{2\pi x}{\Lambda_0}\right) = 0)$:

$$\int_{-\frac{\lambda}{2}}^{\frac{\lambda}{2}} \ln\left[\alpha\cos\left(\frac{2\pi x}{\Lambda_0}\right) + \alpha + 1\right]\ dx \simeq \lambda\alpha - \frac{3\lambda\alpha^2}{4} \tag{78}$$

Therefore, the expression of the resolved shear stress, Eq. (76), can be rewritten as follows.

$$\tau = \mu\overline{\gamma} + \frac{\mu\gamma_0}{L}\left[\Lambda_0\frac{|\tau| - \tau_0}{\Delta\tau} - \frac{3\Lambda_0\left[\frac{\tau-\tau_0}{\Delta\tau}\right]^2}{4}\right] \tag{79}$$

This equation is quadratic in terms of the resolved shear stress variable, τ, and has two solutions, given by the following expressions.

$$\tau = \frac{-2\ \Delta\tau^2\ L + 2\ \Delta\tau\ \gamma_0\Lambda_0\mu + 3\gamma_0\Lambda_0\mu\tau_0 \pm 2\sqrt{\Delta\tau^2\left(\Delta\tau^2L^2 - 2\ \Delta\tau L\gamma_0\Lambda_0\mu + \gamma_0\Lambda_0\ \mu\left(3L\overline{\gamma}\mu + \gamma_0\Lambda_0\mu - 3L\tau_0\right)\right)}}{3\gamma_0\Lambda_0\mu} \tag{80}$$

The yield surface is expressed in terms of the Cauchy stress tensor, as shown in Eq. (57), to estimate the lattice rotation angle within the ideal kink band.

$$\mu\left[\frac{du}{dx} - \gamma\right] = -\left(\frac{\Lambda_0}{2\pi}\right)^2\left(\frac{\Delta\tau}{\gamma_0}\right)\exp\left(-\frac{\gamma}{\gamma_0}\right)\frac{d^2\gamma}{dx^2} + \tau_0 - \Delta\tau\left[1 - \exp\left(-\frac{\gamma}{\gamma_0}\right)\right] \tag{81}$$

By assuming that all terms on the right-hand side of Eq. (81) are negligible compared to the shear modulus, it follows that $\frac{du}{dx} - \gamma \simeq 0$. Furthermore, since the rotation axis of the crystal is normal to the plane of the ideal kink band $(\underline{e}_1 \otimes \underline{e}_2)$, the lattice rotation angle within the kink band can be approximated by the shear strain in the ideal kink band.

$$\text{Skew}\left(\left(\nabla\underline{u}\right)^e\right) = \gamma\left(\underline{e}_2 \otimes \underline{e}_1 - \underline{e}_1 \otimes \underline{e}_2\right) \simeq \theta\left(\underline{e}_2 \otimes \underline{e}_1 - \underline{e}_1 \otimes \underline{e}_2\right) \Rightarrow \theta = \|\overset{\times}{\underline{\omega}}\| \simeq \gamma \tag{82}$$

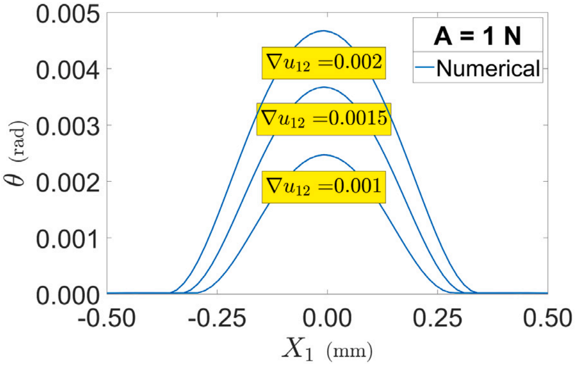

Fig. 2. Classical-SGCP: Rotation field in ideal kink band during different steps of the simple shear loading.

3.2. Single crystal under shear loading: FFT method vs. analytical solution

An ideal kink band, designed as an isotropic elasto-viscoplastic single crystal with a single slip system $\left(\underline{e}_1, \underline{e}_2\right)$ and dimensions of 1 mm×1 mm, is considered to compare the results obtained from the FFT method with those from the proposed analytical solution. For this purpose, the crystal is discretized into 128 × 128 voxels, with the Young's modulus $E = 100$ GPa, Poisson's ratio $\nu = 0.3$ for the elastic deformation part. The initial yield stress is chosen to be small, $\tau_0 = 10$ MPa, and the exponential softening parameters corresponding to the critical resolved shear stress (Eq. (28)) are $\Delta\tau = 15$ MPa and $\gamma_0 = 0.01$. A defect is introduced at the center of the crystal to trigger the localization, with the initial yield stress set to $\tau_0^{\text{defect}} = 0.99 \times \tau_0$. The crystal is subjected to simple shear with an amplitude of $\nabla \underline{u}_{xy} = 0.002$ and a low shear strain rate of 10^{-6} s^{-1}.

Initially, the Classical-SGCP model, with a fixed length scale $A = 1$ N, is employed to obtain the behavior of this crystal. As shown in Fig. 2, the rotation field along the X_1 axis is plotted at different deformation stages. This result demonstrates that in the Classical-SGCP model, the width of the kink band grows fictitiously with deformation. It is expected that after a certain point in the deformation, the kink band will disappear, and a homogeneous field will emerge. Additionally, the figure shows that the peak of the localization becomes increasingly smoother during the deformation.

Fig. 3 illustrates the distributions of the shear strain and rotation angle at the end of the deformation ($\nabla u_{12} = 0.002$). The results confirm that, in the Classical-SGCP model with a fixed length scale, a rotation field aligns with the kink band, while the shear strain is aligned with the slip band direction. Consequently, this model causes the kink band to break into a bundle of slip bands.

Fig. 4 compares the results obtained from the FFT method and the analytical solutions developed in Section 3.1. Two different length scales, $\Lambda_0 = 0.3$ mm and $\Lambda_0 = 0.6$ mm, are considered for the comparison. For both length scales, the results show a high level of agreement between the FFT method and the analytical solutions,[8] validating the implementation of the Enhanced-SGCP theory within the FFT method (see pseudo code of FFT-algorithm in Table 1). Specifically, the comparison shows that during deformation, the width of the kink band remains fixed and precisely equal to the length scale, Λ_0. Another important observation is the intensification of slip within the kink band during deformation.

Fig. 5 presents the distributions of the rotation field for different length scales at the end of the deformation ($\nabla u_{12} = 0.002$) using the Enhanced-SGCP theory. Similar to the Classical-SGCP model with a fixed length scale, the rotation field is aligned with the ideal kink band and is homogeneous in the direction normal to the slip plane (X_2). For $\Lambda_0 = 0.3$ mm, a highly localized rotation field is obtained, efficiently regularized within the kink band, whereas for the larger length scale $\Lambda_0 = 0.6$ mm, a smoother field is observed within the kink band.

The distributions shown in Fig. 6 further demonstrate that the kink band breaks and transforms into a bundle of slip bands, as seen in the Classical-SGCP model. An important finding is that the Enhanced-SGCP theory effectively produces ellipsoidal slip bands by breaking the kink band, whereas the result in the Classical-SGCP model remains unstable, with the slip bands forming straight lines (one voxel width). Additionally, the results from the Enhanced-SGCP theory show that the model regularizes the (transferred) slip bands even in highly localized situations, such as when $\Lambda_0 = 0.3$ mm. As the length scale increases from $\Lambda_0 = 0.3$ mm to $\Lambda_0 = 0.6$ mm, the number of slip bands decreases (per unit length), as a larger length scale provides a smoother field compared to a smaller one.

4. Polycrystalline aggregates

This section presents the results on a periodic Voronoi tessellation of a polycrystalline aggregate with high resolution. Two types of polycrystalline aggregates are considered: two-dimensional and three-dimensional polycrystals. The grains within the Voronoi tessellation are randomly oriented, and the tessellation is generated using an in-house code (Quey et al., 2011). All simulations

---

[8] It is believed that the FFT-based solution offers superior accuracy and better fidelity to the governing constitutive and balance equations, due to applying assumptions in the analytical solution.

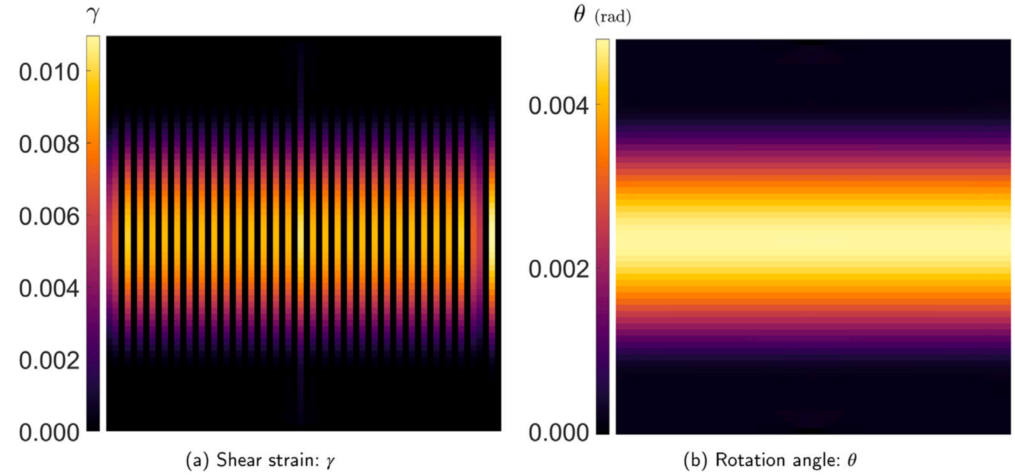

(a) Shear strain: γ (b) Rotation angle: θ

Fig. 3. Classical-SGCP: Distribution of the shear strain and rotation field in ideal kink band at the end of deformation $\nabla u_{12} = 0.002$. A fixed length scale set to $A = 1$ N.

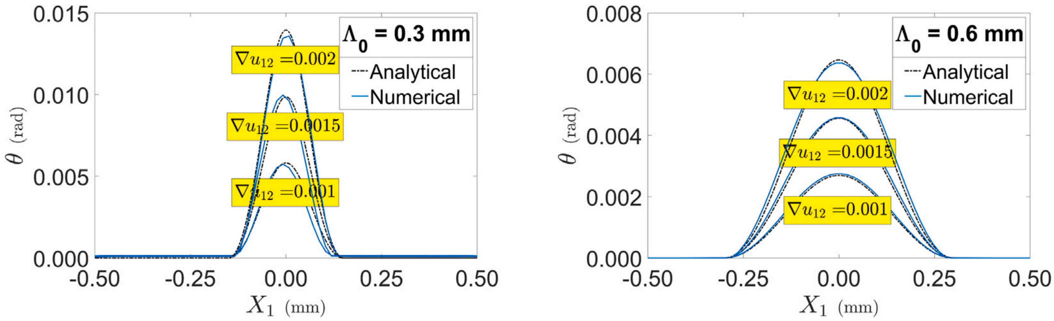

Fig. 4. Enhanced-SGCP: Comparison of the result from FFT method with analytical solutions.

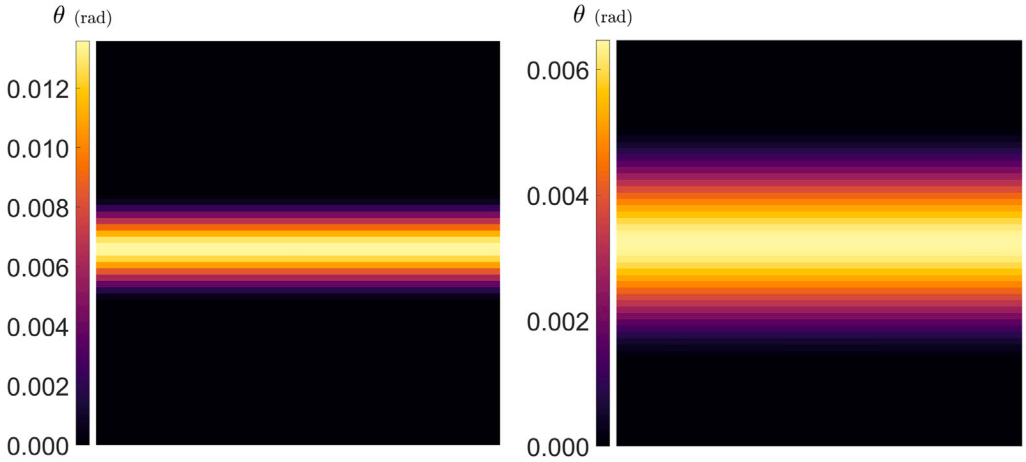

(a) $\Lambda_0 = 0.3$ mm (b) $\Lambda_0 = 0.6$ mm

Fig. 5. Enhanced-SGCP: Distribution of the rotation field in the ideal kink band for different length scales at the end of deformation $\nabla u_{12} = 0.002$.

are subjected to tensile loading at a low strain rate of 10^{-6} s^{-1}, which necessitates the application of mixed boundary conditions in the FFT method (Lame Jouybari et al., 2024). The primary objectives of this section are to investigate the application of the Enhanced-SCGP theory within polycrystalline simulations using the proposed FFT method, with a focus on reproducing shear bands. The comparison between the Enhanced-SGCP and Classical-SGCP theories is also conducted. Additionally, the distinction between

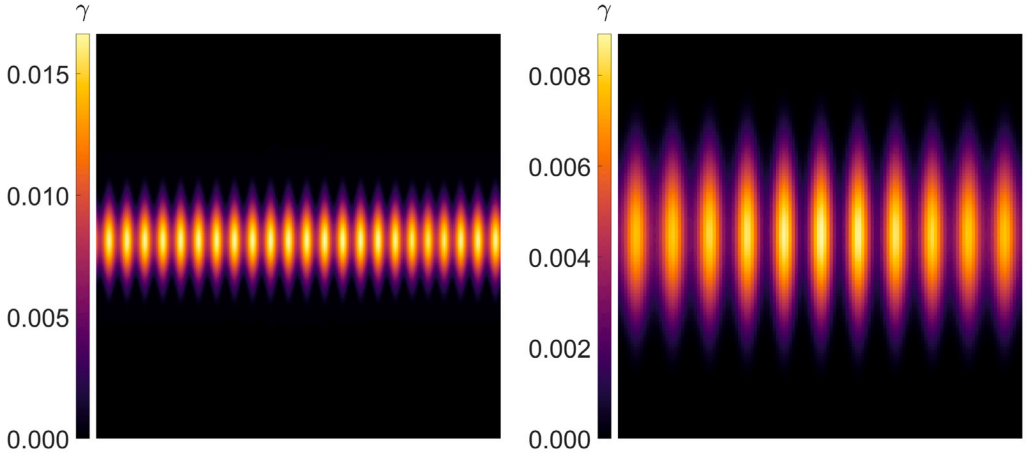

(a) $\Lambda_0 = 0.3$ mm (b) $\Lambda_0 = 0.6$ mm

Fig. 6. Enhanced-SGCP: Distribution of the shear strain in the ideal kink band for different length scales at the end of deformation $\nabla u_{12} = 0.002$.

Table 3
Elastic and plastic properties of the two-dimensional and three dimensional polycrystalline aggregates.

	E	ν	K	n	τ_0	$\Delta\tau$	γ_0
Two-dimensional aggregate	100 GPa	0.3	10 MPa s^{-n}	15	100 MPa	50 MPa	0.05
Three-dimensional aggregate	100 GPa	0.3	10 MPa s^{-n}	15	100 MPa	50 MPa	0.10

slip and kink bands is analyzed, and the influence of the Enhanced-SGCP theory on the formation of kink bands is examined. The evolution of different length scales during deformation is explored, and the role of grain boundaries in the transmission of deformation bands between neighboring grains is also discussed. Finally, the evolution of the back-stress and generalized back-stress throughout the deformation process is analyzed.

4.1. Two-dimensional aggregate

This section investigates a two-dimensional periodic Voronoi tessellation of a polycrystalline aggregate consisting of 1800 columnar grains, each equipped with an in-plane slip system and aligned with the grain orientation. The aggregate has a total length of 10 mm $\times$ 10 mm, and its microstructure is depicted in Fig. 7 . The mean grain size is estimated[9] by $\mathrm{GS}_{2D} = 0.235$ mm. The microstructure is discretized into a high-resolution grid of approximately 4 million voxels, or 2048 × 2048 voxels in total. The elasto-viscoplastic behavior of the microstructure is considered in the mechanical analysis, with the material properties summarized in Table 3. To investigate the Enhanced-SGCP theory, two different length scales are chosen based on the threshold criterion introduced in Appendix E for the simulations: $\Lambda_0 = 0.1$ mm and $\Lambda_0 = 0.15$ mm. Additionally, three types of grain boundaries are incorporated as higher-order interface conditions, namely, MicroFree, MicroContinuity, and MicroHard. The corresponding FFT-algorithm for this theory is detailed in Table 1. In all simulations of this section, the microstructure is subjected to tensile loading along the y-axis, with a total amplitude of $\nabla u_{yy} = 0.02$.

Fig. 8 presents the spatially averaged evolution of macroscopic variables during the applied loading, including the tensile component of the Cauchy stress, back-stress, generalized back-stress, Nye tensor, and higher-order modulus, as incorporated within the Enhanced-SGCP theory. In this figure, the CCP framework is represented by the length scale parameter $\Lambda_0 = 0$ mm, which inherently results in vanishing back-stress, generalized back-stress, and higher-order modulus throughout the loading process. Notably, in this framework, the Nye tensor evolution exhibits a linear increase, indicating that the formation of the GNDs leads to instability. This instability arises due to the absence of back-stress and generalized back-stress, which otherwise would counteract with linear multiplication of the GND density. The second column of the figure illustrates the evolution of the macroscopic variables for a length scale of $\Lambda_0 = 0.1$ mm, providing a comparative analysis between the CCP framework and the Enhanced-SGCP theory, along with the effects of grain boundaries. The macroscopic stress–strain response at this length scale demonstrates that activating the Enhanced-SGCP theory introduces additional hardening which is physically interpreted as the accumulation and pile-up of GNDs (Lame Jouybari et al., 2024). This increased hardening is governed by the evolution of back-stress and generalized back-stress, both of which are embedded within the shear flow rule, as formulated in Eq. (26). Furthermore, the transition from purely elastic macroscopic behavior to plastic deformation is significantly smoother in the Enhanced-SGCP theory, whereas in the CCP framework, this transition occurs abruptly. This distinction suggests that, at the onset of macroscopic yielding, CCP-based simulations exhibit

---

[9] $\mathrm{GS}_{2D} = \sqrt{\frac{L^2}{N_g}}$ where L is the total length of the microstructure and N_g is the number of the grains.

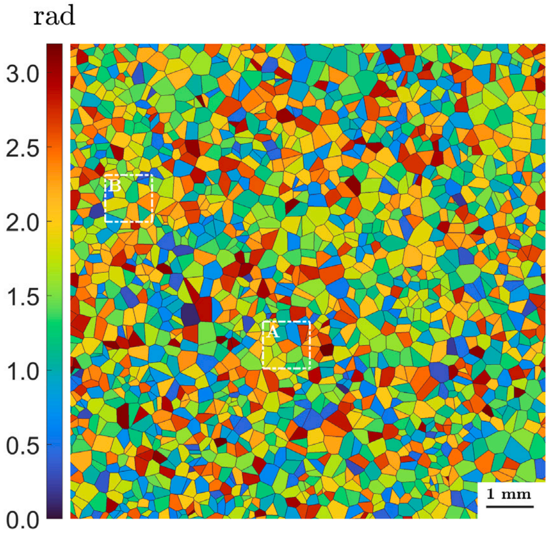

Fig. 7. Microstructure of the two-dimensional polycrystalline aggregate composed of 1800 columnar grains: colors represent the orientation of the grains with respect to the loading direction and black lines correspond to the grain boundary voxels. Squares A and B denote two specific regions used later in the analysis.

higher instability. Additionally, the results reveal that the MicroHard condition induces the highest hardening response, while the MicroFree condition results in the lowest hardening. This trend is attributed to their respective microstructural descriptions. Specifically, the evolution of back-stress in the MicroHard condition is significantly higher than in the other cases, while in the MicroFree and MicroContinuity conditions, the rate of back-stress accumulation is lower and eventually saturates during loading. Furthermore, the rate of GND density multiplication (or Nye tensor evolution) increases nonlinearly across all conditions but remains lower than in the CCP framework. This finding confirms that the Enhanced-SGCP theory effectively regulates GND multiplication during applied loading. Moreover, in the MicroFree and MicroContinuity conditions, where shear bands can propagate across grain boundaries, the GND density is higher than in the MicroHard condition, where grain boundary resistance suppresses transmission. Importantly, the last plot in Fig. 8 shows that the higher-order modulus decreases upon the initiation of plastic deformation. During subsequent loading, the rate of this reduction diminishes and eventually stabilizes. This observation confirms that the proposed Enhanced-SGCP theory appropriately accounts for the higher-order modulus as a function of the length scale and microstructural properties, demonstrating that it is not a constant material parameter. Instead, as plastic deformation and loading increase, the modulus decreases and eventually saturates, thereby limiting the influence of strain gradient effects at high deformation levels. The third column of Fig. 8 presents the evolution of macroscopic variables for a length scale of $\Lambda_0 = 0.15$ mm. The results indicate that increasing Λ_0 leads to more pronounced hardening behavior across all grain boundary conditions compared to the lower length scale ($\Lambda_0 = 0.1$ mm). In this case, higher back-stress and generalized back-stress values develop during deformation, which further suppresses GND density multiplication (Nye tensor evolution) and enhances the reduction of the higher-order modulus.

Fig. 9 illustrates the evolution of stress concentration in both the bulk material and along grain boundaries. In the bulk, stress concentration is quantified by the volume fraction of material where the von Mises stress exceeds twice the average von Mises stress, Eq. (83). For grain boundaries, it is measured by the surface fraction of grain boundaries experiencing von Mises stress greater than twice the average, Eq. (84).

$$\phi_{\text{Bulk}} = \frac{1}{V}\int_{\{x\in\mathcal{B}|\sigma_{\text{vm}}(x)>2\overline{\sigma_{\text{vm}}}\}} dV \tag{83}$$

$$\phi_{\text{GB}} = \frac{1}{S}\int_{\{x\in\partial\mathcal{B}|\sigma_{\text{vm}}(x)>2\overline{\sigma_{\text{vm}}}\}} dS \tag{84}$$

The volume fraction curves in Fig. 9 reveal that following the onset of plastic deformation, the volume fraction experiences a gradual increase during applied loading. Initially, at the onset of loading, all grains undergo purely homogeneous elastic deformation, resulting in a zero stress concentration. In this plot, the CCP framework exhibits a slightly higher volume fractions, whereas the MicroHard condition results in slightly lower volume fractions. At final deformation and across all conditions, only 5%–7% of the microstructure experiences von Mises stress concentration.

The surface fraction of the von Mises stress at grain boundaries follows a similar trend. At the initial stage of applied loading, no stress concentration is observed at the grain boundaries. However, upon the initiation of plastic deformation, the von Mises stress localizes at the grain boundaries at levels significantly higher than within the grains. Notably, in the case of the MicroHard condition the surface fraction exceeds 30% at the final deformation. Observation suggests that the strong resistance to slip transmission at grain boundaries, significantly contributes to the development of large local stress, potentially leading to micro-crack initiation in irradiated material with oxidized grain boundaries (IASCC) (McMurtrey et al., 2011).

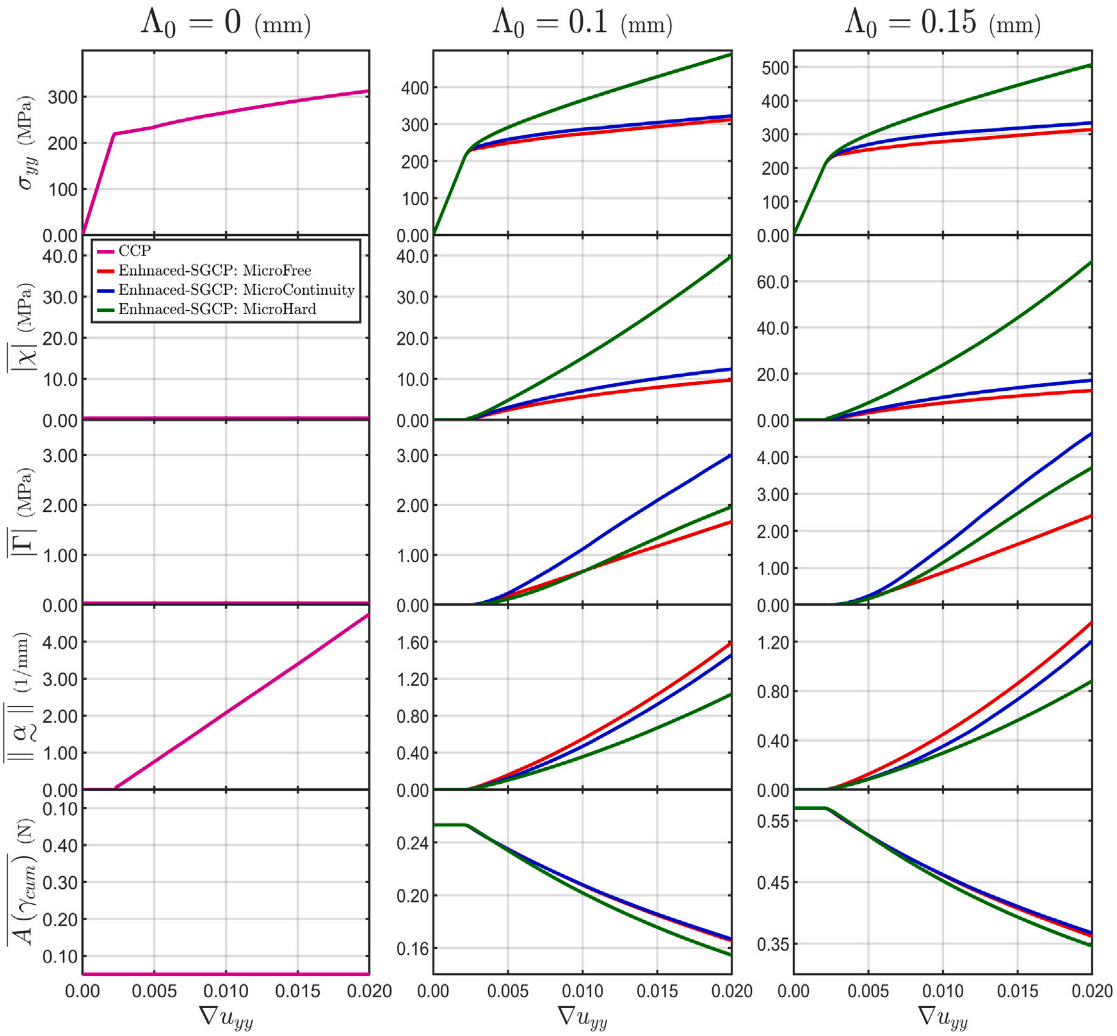

Fig. 8. Evolution of the spatially averaged tensile component of the Cauchy stress, σ_{yy}, along with the back-stress, $\overline{|\chi|}$, generalized back-stress, $\overline{|\Gamma|}$, norm of the Nye tensor, $\overline{\|\alpha\|}$, and higher-order modulus, $\overline{A(\gamma_{cum})}$, during applied loading. Results are obtained from the CCP framework and the Enhanced-SGCP theory for different length scales, Λ_0, and varying higher-order interface conditions at the grain boundary.

Fig. 10 presents the distribution of the norm of the plastic distortion tensor, Eq. (3), and the rotation field, Eq. (6), obtained from the simulation within the CCP framework. The results indicate that plastic deformation and the rotation field are highly localized along narrow, straight bands within the grains, commonly referred to as shear bands. Since each grain contains only single in-plane slip system, two perpendicular bands emerge within the grains: one exhibiting a localized rotation angle, referred to as kink band, and another without significant rotation localization, known as slip band (Asaro and Rice, 1977). This observation confirms that the CCP framework successfully reproduces both slip and kink bands in approximately the same amount. Typically, these bands are localized within one or two voxels, leading to the conclusion that the results from the CCP framework are unstable and voxel-dependent (Lame Jouybari et al., 2024). Furthermore, the right side of the figure focuses on a subregion of the microstructure containing approximately ten grains, illustrating the evolution of these fields at three distinct stages of applied loading: $\nabla u_{yy} = 0.004$, $\nabla u_{yy} = 0.012$, and $\nabla u_{yy} = 0.02$. It is evident that as the applied loading progresses, the number of bands increases, and interactions between them occur, allowing the bands to propagate and transmit across grain boundaries.

Fig. 11 illustrates the distributions of the norm of the plastic distortion tensor, Eq. (3), and the rotation field, Eq. (6), as obtained from simulations within the Enhanced-SGCP theory under the MicroFree condition at the grain boundaries. The distribution of the norm of the plastic distortion tensor reveals that within each grain, plastic localization occurs predominantly along a single preferred direction, forming slip bands. The primary distinction between the distributions obtained from the Enhanced-SGCP theory and those from the CCP framework is that the kink bands present in the CCP framework are eliminated and replaced by multiple equidistant parallel slip bands in the grains. This observation suggests that the Enhanced-SGCP theory disrupts the equivalence between slip and kink bands, leading to an increased number of slip bands within the microstructure. As discussed in Section 3.1, the proposed theory

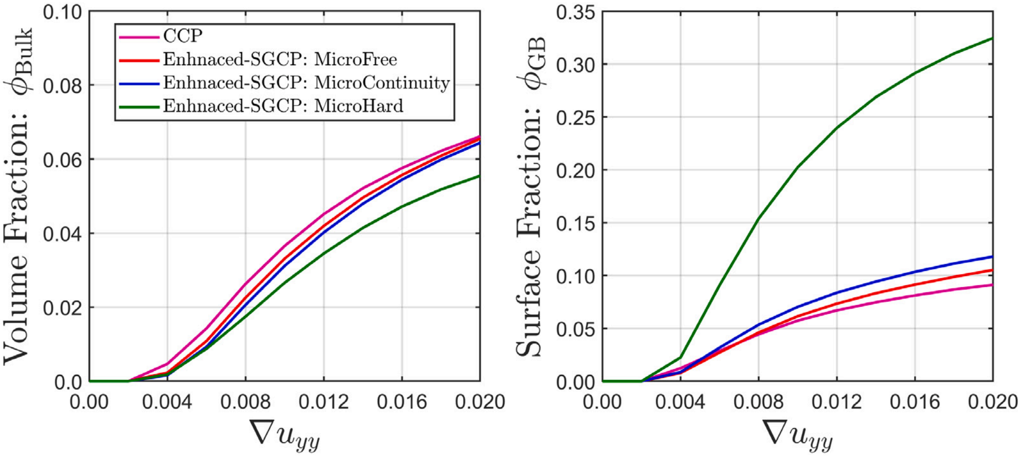

Fig. 9. Evolution of stress concentrations in the two-dimensional microstructure during applied loading, highlighting regions where the von Mises stress is concentrated within the grains and along the grain boundaries. The results are obtained from the CCP framework and the Enhanced-SGCP theory, considering a length scale of $\Lambda_0 = 0.1$ mm and different higher-order interface conditions at the grain boundary.

does not directly influence slip bands but primarily acts on kink bands. Consequently, by comparing the rotation field distributions in this figure with those in Fig. 10 from the CCP framework, it is evident that the width of the kink bands is regularized, attaining a finite amplitude approximately equal to the length scale parameter, Λ_0. This result is consistent with expectations for a polycrystalline aggregate under tensile loading, where local shear loading may arise due to interactions with neighboring grains. Hence, similar behavior is observed in single crystalline simulations under shear loading, as discussed in Section 3.2. Accordingly, the width of the rotation field also aligns closely with the characteristic length scale. Another important distinction emphasized here is that, within each grain, plastic localization consistently follows a single preferred direction in the form of slip bands. However, subtle differences exist among these slip bands. Some of them correspond to the original slip bands already reproduced by the CCP framework. These original slip bands typically propagate freely across adjacent grains due to the MicroFree condition on the grain boundaries, maintaining a width on the order of one or two voxels, and remain uninfluenced by the Enhanced-SGCP theory. Additionally, the distributions in this figure reveal the presence of another type of slip band, characterized by a finite width approximately equal to the length scale amplitude and a shorter width compared to the original slip bands. These bands originate from kink bands that have been transformed into multiple slip bands with a regularized rotation field by the Enhanced-SGCP theory. Here, these bands are referred to the "transferred slip bands”. Furthermore, to illustrate the local behavior at different length scales and different stages of applied loading, the same microstructural region as in Fig. 10 is selected. The results demonstrate that, throughout the applied loading process, the Enhanced-SGCP theory effectively maintains the localization characteristics. As the length scale increases, the transferred slip bands widen, and their associated rotation fields become smoother and regularized.

Fig. 12 presents the distributions of the norm of the plastic distortion tensor, Eq. (3), and the rotation field, Eq. (6), obtained from simulations within the Enhanced-SGCP theory under the MicroHard condition at the grain boundaries. Similar to the MicroFree condition, the kink bands observed in the CCP framework (Fig. 10) are replaced by multiple slip bands with a finite width approximately equal to the length scale parameter, Λ_0. A key distinction between the MicroHard and MicroFree conditions corresponds to the flow of the original slip bands. Under the MicroHard condition, slip bands cannot propagate across grain boundaries; instead, they terminate upon reaching the boundary. Thus increasing the local stress as discussed in Fig. 9. Consequently, this restriction leads to the formation of a greater number of intragranular slip bands compared to the MicroFree condition.

Fig. 13 presents the distributions of variables associated with the Enhanced-SGCP theory in a specific region B of the microstructure shown in Fig. 7. The selected variables include the norm of the plastic distortion tensor, $\|(\nabla \underline{u})^p\|$, rotation field, θ, back-stress, χ, von Mises stress, σ_{vm}, higher-order modulus, $A(\gamma_{cum})$, norm of the Nye tensor, $\|\underset{\sim}{\alpha}\|$, generalized back-stress, Γ, and critical resolved shear stress, τ_{cr}. These distributions correspond to the MicroHard condition at the grain boundaries with a length scale of $\Lambda_0 = 0.1$ mm. The distribution of the norm of the plastic distortion tensor reveals that all bands are aligned parallel within each grain. Regions exhibiting a high concentration of the rotation field (those also exhibiting finite Nye tensor distributions) show increased plastic deformation localization, indicating that these regions correspond to the interaction and overlap of original slip bands and transferred slip bands. In particular, within regions where plastic deformation is highly localized, the critical resolved shear stress decreases from its initial value, $\tau_0 = 100$ MPa. This reduction demonstrates the underlying mechanism of defect sweeping along the dislocation glide paths, which is a defining characteristic of clear channel formation in irradiated microstructures. Furthermore, the distribution of the higher-order modulus demonstrates that in regions where plastic deformation is localized, the modulus undergoes reduction compared to other areas. This localized decrease is particularly evident within shear bands, also referred to as clear channels, and is directly linked to the underlying deformation mechanism. As previously described, the acceleration of dislocation glide during plastic flow facilitates the removal of irradiation-induced defects such as Frank loops. This sweeping away of hardening obstacles within the clear channels leads to a local softening of the material response. Consequently,

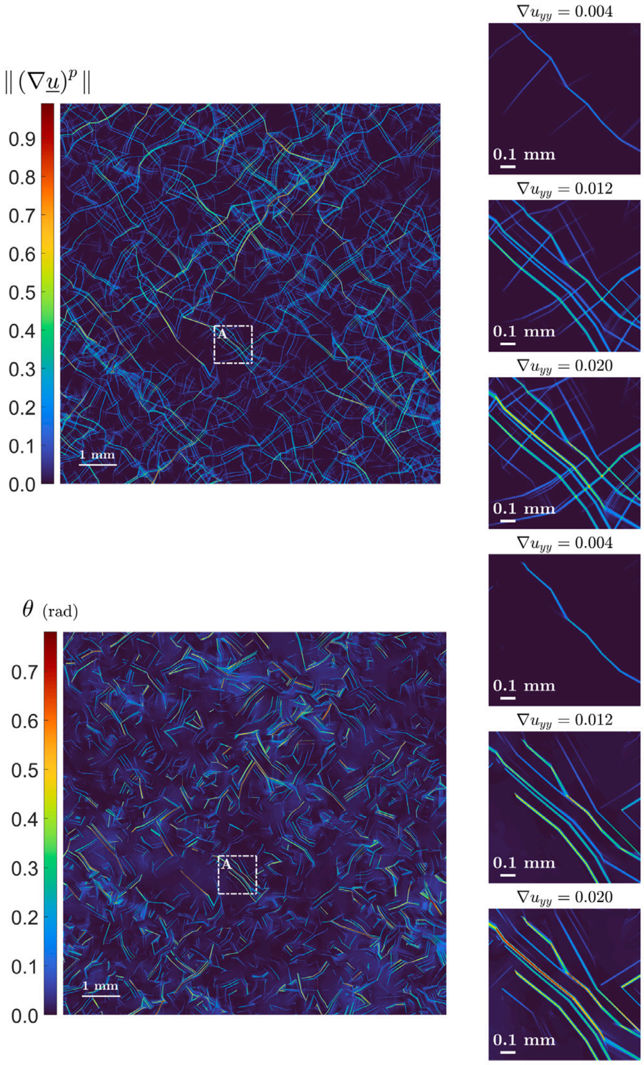

Fig. 10. Distributions of the norm of the plastic distortion tensor, $\|(\nabla \underline{u})^p\|$, and the rotation field, θ, in the two-dimensional microstructure, obtained from the CCP framework at final stage of the deformation $\nabla u_{yy} = 0.02$. The insets highlight a specific region of the microstructure, containing approximately ten grains, illustrating the evolution of these distributions at three loading steps: $\nabla u_{yy} = 0.004$, $\nabla u_{yy} = 0.012$, and $\nabla u_{yy} = 0.02$.

the rate of the additional hardening contributions introduced by Enhanced-SGCP theory, such as the back-stress and generalized back-stress terms within the shear flow rule, Eq. (26), are effectively diminished in these regions by the reduction of the higher-order modulus during the deformation. This characteristic is a key distinction of the proposed Enhanced-SGCP theory relative to classical theories, as it ensures the persistence of localization regions throughout the applied loading process. Additionally, the von Mises stress distribution reveals a significant concentration along the GNDs or the Nye tensor in these regions, further validating the theoretical framework.

4.2. Three-dimensional aggregate

In this section, a three-dimensional periodic Voronoi tessellation is employed to generate a polycrystalline aggregate consisting of 64 randomly oriented FCC grains, with an overall microstructure size of $1\ \mathrm{mm} \times 1\ \mathrm{mm} \times 1\ \mathrm{mm}$ and mean grain size[10] of $\mathrm{GS}_{3D} = 0.25$ mm. Each grain possesses up to 12 potential slip systems for dislocation glide, characterized by the Miller indices $\{111\}\langle 110\rangle$. These slip systems, defined in the reference configuration, are rotated according to the respective grain orientations. The resulting microstructure is depicted in Fig. 14. It is discretized into a structured grid of $200 \times 200 \times 200$ voxels, leading to a

---

[10] $\mathrm{GS}_{3D} = \sqrt[3]{\frac{L^3}{N_g}}$.

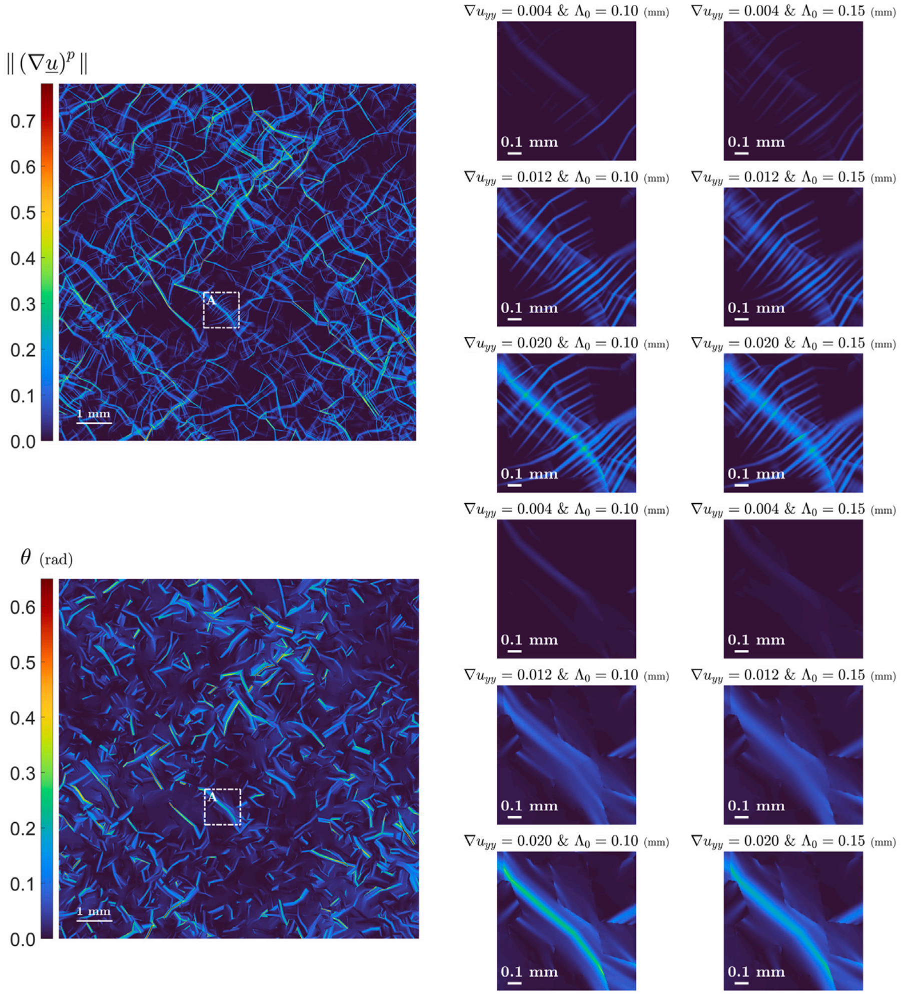

Fig. 11. Distributions of the norm of the plastic distortion tensor, $\|(\nabla \underline{u})^p\|$, and the rotation field, θ, in the two-dimensional microstructure at final stage of the deformation $\nabla u_{yy} = 0.02$, obtained from the Enhanced-SGCP theory with a length scale of $\Lambda_0 = 0.1$ mm and the MicroFree condition at the grain boundary. The insets highlight a specific region of the microstructure same as in Fig. 10, illustrating the evolution of these distributions for two different length scales, $\Lambda_0 = 0.1$ mm and $\Lambda_0 = 0.15$ mm, at three loading steps: $\nabla u_{yy} = 0.004$, $\nabla u_{yy} = 0.012$, and $\nabla u_{yy} = 0.02$.

total of 8 million voxels. The aggregate is subjected to uniaxial tensile loading along the z-direction, with a prescribed final strain amplitude of $\nabla u_{zz} = 0.01$ and a low strain rate of 10^{-6} s^{-1}. The material properties used in the simulations[11] are summarized in Table 3. Furthermore, the Enhanced-SGCP theory is considered, with the corresponding FFT-based numerical algorithm outlined in Table 1. The results obtained using this approach are systematically compared with those from the CCP framework, considering different higher-order interface conditions at the grain boundaries. To investigate the influence of length scale effects, simulations are conducted for two characteristic length scales, $\Lambda_0 = 0.05$ mm and $\Lambda_0 = 0.1$ mm, satisfying the threshold criterion given in Appendix E.

Fig. 15 presents the evolution of several key macroscopic and microscopic variables during the applied loading, as obtained from simulations using both the CCP framework and the Enhanced-SGCP theory. Specifically, the figure illustrates the macroscopic tensile component of the Cauchy stress tensor, the spatially averaged back-stress across all slip systems, the spatially averaged generalized back-stress, the norm of the Nye tensor, and the spatially averaged higher-order modulus across all slip systems. These results are analyzed for different grain boundary conditions and length scales. The first column of Fig. 15 corresponds to the CCP framework. The stress–strain curve indicates that, following the onset of plastic deformation (i.e., after exceeding the macroscopic yield stress), the hardening behavior is primarily governed by the microstructure. This continues until the macroscopic stress reaches a peak, after which macroscopic softening is initiated. Notably, the rate of softening accelerates as loading progresses. The second column

---

[11] In the three-dimensional simulations, the softening rate parameter γ_0 is selected to be twice the value employed in the two-dimensional simulations. This adjustment aims to mitigate numerical instabilities associated with macroscopic softening behavior within the CCP framework. The need for a higher softening rate in 3D arises due to the activation of up to 12 potential slip systems available for dislocation glide.

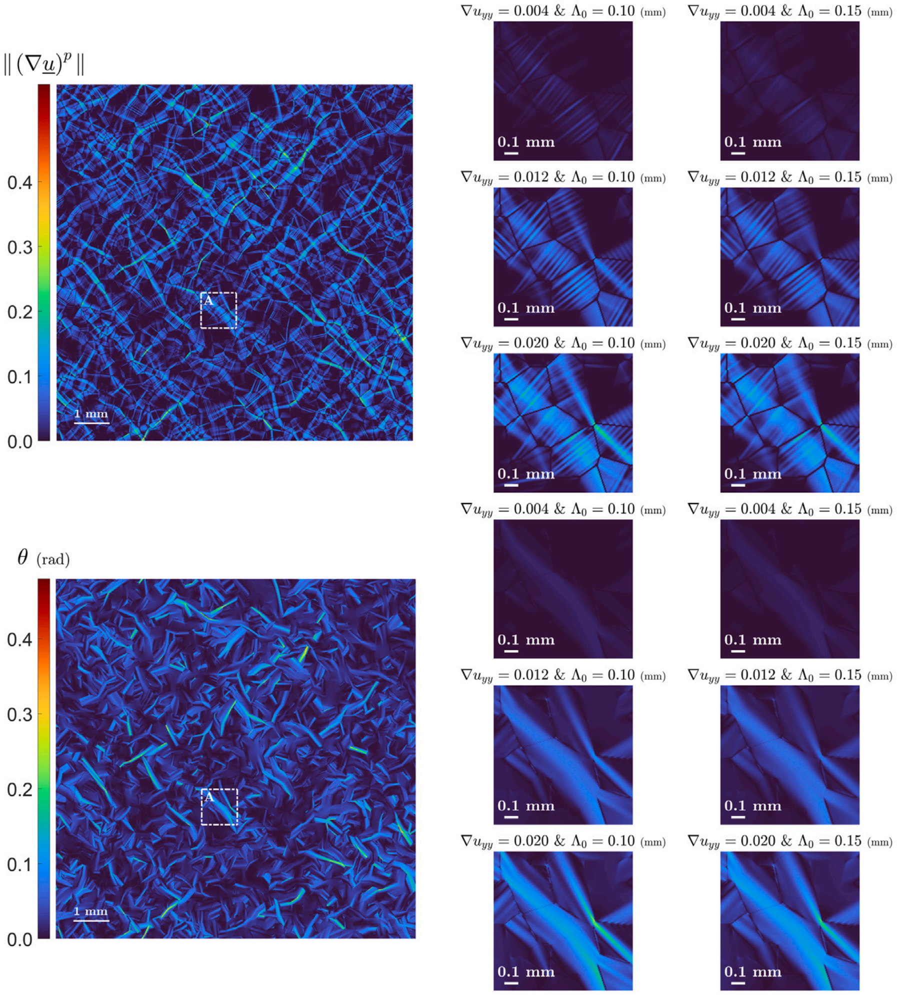

Fig. 12. Distributions of the norm of the plastic distortion tensor, $\|(\nabla \underline{u})^p\|$, and the rotation field, θ, in the two-dimensional microstructure at final stage of the deformation $\nabla u_{yy} = 0.02$, obtained from the Enhanced-SGCP theory with a length scale of $\Lambda_0 = 0.1$ mm and the MicroHard condition at the grain boundary. The insets highlight a specific region of the microstructure same as in Fig. 10, illustrating the evolution of these distributions for two different length scales, $\Lambda_0 = 0.1$ mm and $\Lambda_0 = 0.15$ mm, at three loading steps: $\nabla u_{yy} = 0.004$, $\nabla u_{yy} = 0.012$, and $\nabla u_{yy} = 0.02$.

presents results for a length scale of $\Lambda_0 = 0.05$ mm under different grain boundary conditions. The stress–strain curves reveal that the MicroFree and MicroContinuity conditions exhibit similar mechanical responses. Compared to the CCP framework, in regions where macroscopic softening occurs in the CCP case, the rate of hardening is reduced under the MicroFree and MicroContinuity conditions. However, under the MicroHard condition, the highest level of hardening behavior is observed. Consequently, the evolution of the back-stress remains elevated throughout the loading process in this case. Additionally, the norm of the Nye tensor evolves differently in the Enhanced-SGCP theory, where the generation and multiplication of the GNDs, quantified through the Nye tensor, are controlled and influenced by both the back-stress and generalized back-stress. In contrast, within the CCP framework, the rate of Nye tensor multiplication increases significantly during loading. The third column of Fig. 15 corresponds to simulations with an increased length scale of $\Lambda_0 = 0.1$ mm. The results indicate that increasing the length scale enhances the hardening response, leading to a more pronounced evolution of both the back-stress and generalized back-stress compared to the lower length scale ($\Lambda_0 = 0.05$ mm). Furthermore, similar to the observations in the two-dimensional simulations (Fig. 8), the higher-order modulus decreases progressively during deformation across all grain boundary conditions.

Fig. 16 presents the distributions of the norm of the plastic distortion tensor and the rotation field at the end of the applied tensile loading. The results are obtained from both the CCP framework and the Enhanced-SGCP theory, considering different higher-order interface conditions at the grain boundaries, namely the MicroFree and MicroHard conditions. Insets (a) and (b) in Fig. 16 correspond to the CCP framework. The results indicate that plastic deformation is highly localized within shear bands, which have a characteristic width of approximately one to two voxels. Furthermore, similar to the two-dimensional simulations shown in Fig. 10, both slip and kink bands are reproduced, typically in an equal ratio. Insets (c) and (d) display the results obtained using

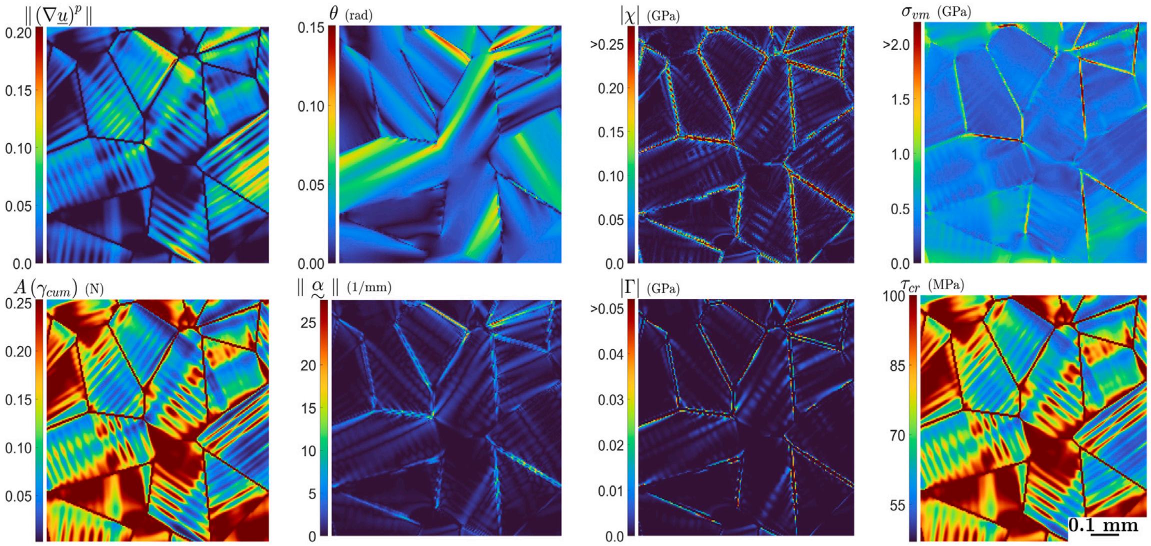

Fig. 13. Distributions of the norm of the plastic distortion tensor, $\|(\nabla \underline{u})^p\|$, the rotation field, θ, back-stress, $|\chi|$, von Mises stress, σ_{vm}, higher-order modulus, $A(\gamma_{\text{cum}})$, norm of the Nye tensor, $\|\underset{\sim}{\alpha}\|$, generalized back-stress, $|\Gamma|$, and critical resolved shear stress, τ_{cr}, in the specific region B of the microstructure shown in Fig. 7, obtained from the Enhanced-SGCP theory with a length scale of $\Lambda_0 = 0.1$ mm and the MicroHard condition at the grain boundary at the end of applied loading, $\nabla u_{yy} = 0.02$.

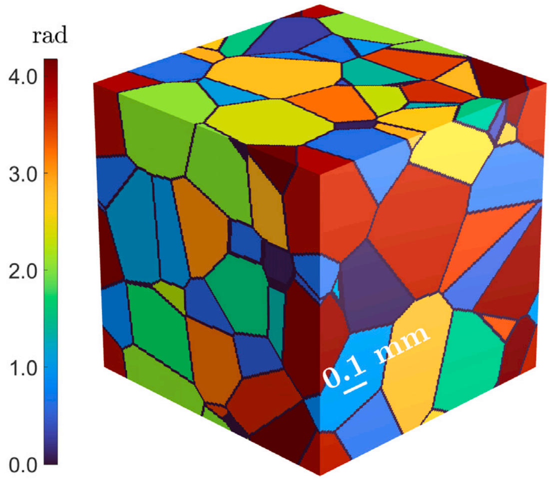

Fig. 14. Microstructure of the three-dimensional polycrystalline aggregate with the length of 1mm × 1mm × 1mm composed of 64 randomly oriented grains: colors represent the orientation of the first Euler angle of the grains and black voxels correspond to the grain boundaries.

the Enhanced-SGCP theory under the MicroFree condition. In this case, the rotation field is smoothly regularized, exhibiting a characteristic width approximately equal to the length scale $\Lambda_0 = 0.05$ mm, in contrast to the sharp localization observed in the CCP framework (inset (b)). Additionally, the distribution of plastic deformation under this condition reveals that the kink bands present in the CCP framework are suppressed by the Enhanced-SGCP theory. As a result, the original slip bands become more pronounced, while new transferred slip bands emerge in parallel within each grain. These transferred slip bands exhibit a lower amplitude and narrower width compared to the original slip bands. Consistent with the two-dimensional simulations, the Enhanced-SGCP theory disrupts the equivalence between slip and kink bands, favoring the formation of slip bands within the grains. A key distinction between the three-dimensional and two-dimensional simulations is the emergence of non-perpendicular and non-parallel shear bands in certain grains. This observation suggests that, in three dimensions, more than one slip system can become activated during plastic deformation in those grains. In contrast, the two-dimensional simulations exhibit plastic localization predominantly along a single preferred intragranular direction. Finally, insets (e) and (f) illustrate the results obtained under the MicroHard condition. Under this condition, the original slip bands are more prominently reproduced, and they propagate until reaching the grain boundaries in contract to the MicroFree condition. Notably, in some grains, a distinct zigzag pattern of parallel bands appears. This pattern

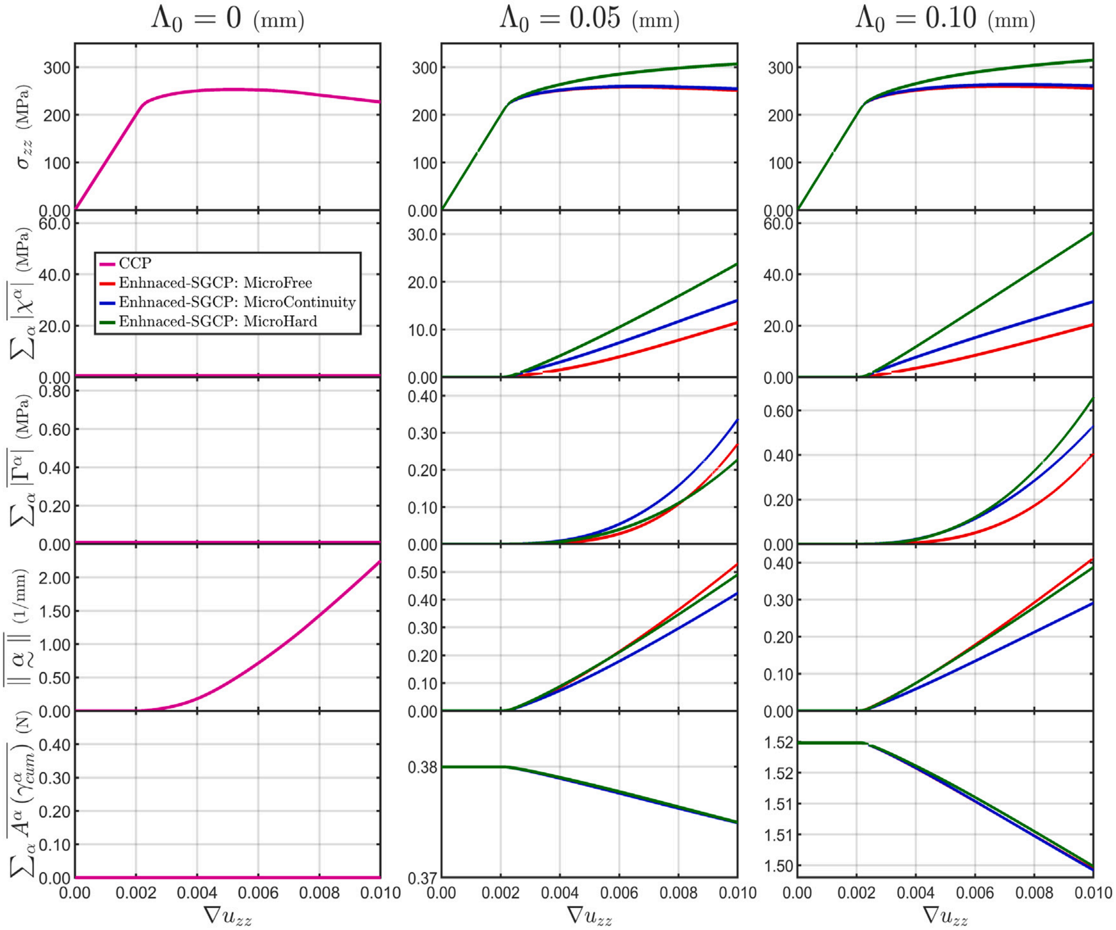

Fig. 15. Evolution of the spatially averaged tensile component of the Cauchy stress, σ_{zz}, along with the back-stress, $\sum_\alpha \overline{|\chi^\alpha|}$, generalized back-stress, $\sum_\alpha \overline{|\Gamma^\alpha|}$, norm of the Nye tensor, $\overline{\|\underset{\sim}{\alpha}\|}$, and higher-order modulus, $\sum_\alpha \overline{A^\alpha\left(\gamma^\alpha_{cum}\right)}$, during applied loading. Results are obtained from the CCP framework and the Enhanced-SGCP theory for different length scales, Λ_0, and varying higher-order interface conditions at the grain boundary.

arises due to the interaction between original slip bands associated with one slip system and transferred slip bands originating from another slip system, highlighting the complex interplay of slip activity at the grain scale.

Fig. 17 further illustrates that, under the MicroHard condition, the von Mises stress is highly concentrated at regions of the grain boundaries where both original and transferred slip bands intersect. As discussed in Fig. 9, this concentration can be interpreted as indicative of the IASCC mechanism in irradiated structural materials with oxidative grain boundaries.

4.3. Discussion: Comparison with classical-SGCP model

To distinguish the key features of the proposed Enhanced-SGCP theory in polycrystalline materials, a comparative analysis is conducted against the Classical-SGCP model, as introduced in Section 2.2. For this purpose, the two-dimensional polycrystalline aggregate, depicted in Fig. 7, is considered. In the Classical-SGCP model, the governing equations include the generalized balance equation (Eq. (33)) and the shear flow rule (Eq. (36)), while numerical implementation follows the FFT-based algorithm outlined in Table 2. In contrast, the Enhanced-SGCP theory employs the generalized balance equation (Eq. (19)), the modified shear flow rule (Eq. (26)), and the FFT algorithm detailed in Table 1. The material properties of the polycrystalline aggregate remain identical in both models, as specified in Table 3. It is important to note that the length scales in the two models have different interpretations and units. To enable a meaningful comparison, the length scale in the Classical-SGCP model is chosen such that it corresponds to the higher-order modulus of the Enhanced-SGCP theory in the elastic regime, as described by Eq. (29). Specifically, the length scale in the Classical-SGCP model is defined as:

$$A^{\text{Classic}} = A^{\text{Enhanced}}\left(\gamma_{\text{cum}} = 0\right) = \left(\frac{\Lambda_0}{2\pi}\right)^2 \frac{\Delta\tau}{\gamma_0} \tag{85}$$

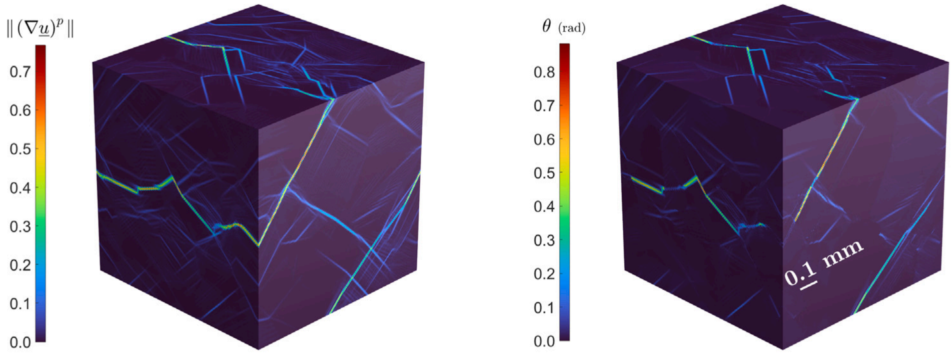

(a) CCP framework: norm of plastic distortion tensor (b) CCP framework: Rotation field

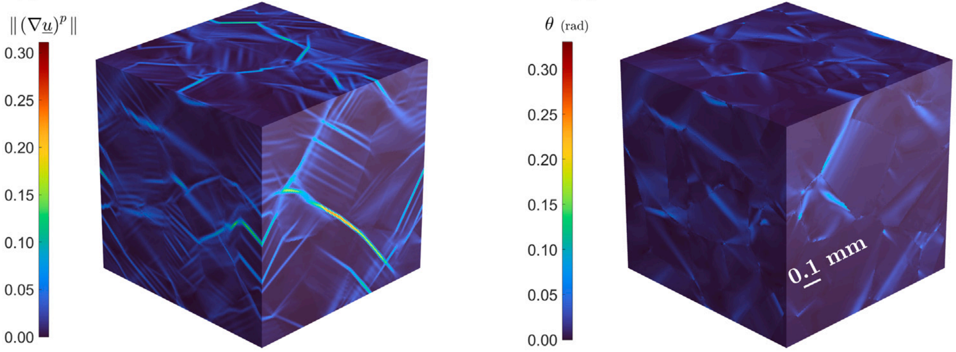

(c) MicroFree condition: norm of plastic distortion tensor (d) MicroFree condition: Rotation field

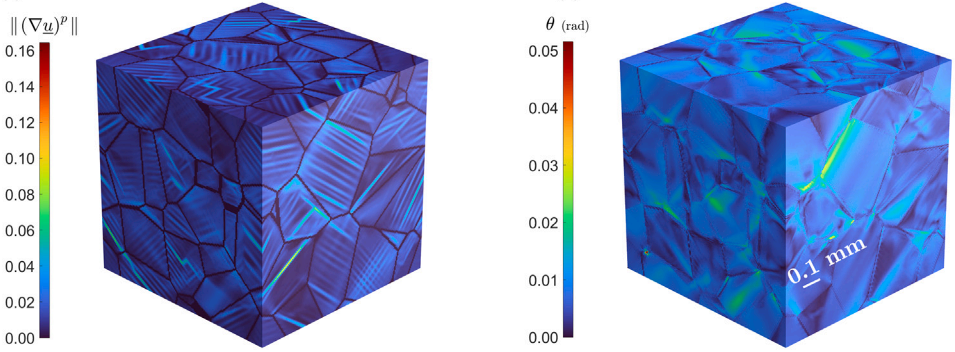

(e)MicroHard condition: norm of plastic distortion tensor (f) MicroHard condition: Rotation field

Fig. 16. Distributions of the norm of the plastic distortion tensor, $\|(\nabla \underline{u})^p\|$, and the rotation field, θ, in the three-dimensional microstructure, obtained from the CCP framework and the Enhanced-SGCP theory with a length scale of $\Lambda_0 = 0.05$ mm and different higher-order interface conditions at the grain boundary at the end of applied loading, $\nabla u_{zz} = 0.01$.

Accordingly, for the simulations, the length scale in the Enhanced-SGCP theory is set to $\Lambda_0 = 0.2$ mm, which results in an equivalent length scale of $A = 1.01$ N in the Classical-SGCP model.

Fig. 18 illustrates the evolution of key macroscopic and microscopic variables during the applied loading, as obtained from simulations using both the Classical-SGCP model and the Enhanced-SGCP theory. Specifically, the figure presents the macroscopic tensile component of the Cauchy stress tensor, the spatially averaged back-stress, the spatially averaged generalized back-stress, the norm of the Nye tensor, and the spatially averaged higher-order modulus (interpreted as the length scale in the Classical-SGCP model). Each column corresponds to a specific higher-order interface condition at the grain boundaries. The first column represents the MicroFree condition. The results indicate that, following the onset of plastic deformation, both models exhibit strain hardening. However, in the Enhanced-SGCP theory, the rate of hardening decreases over the course of loading, whereas in the Classical-SGCP model, it increases monotonically. This behavior in the Classical-SGCP model is attributed to the continuous increasing of back-stress, whereas in the Enhanced-SGCP theory, the back-stress evolution exhibits a reduced growth rate and eventually saturates, inherits the sweeping away of irradiation-induced defects mechanism within the shear bands or clear channels. Consequently, the GNDs in the Classical-SGCP model suppresses more than the Enhanced-SGCP theory. A similar trend is observed under the MicroContinuity and MicroHard conditions. In all cases, a key distinction between the two theories is evident in the evolution of the higher-order modulus. In the Enhanced-SGCP theory, the higher-order modulus decreases with increasing applied loading, effectively mitigating

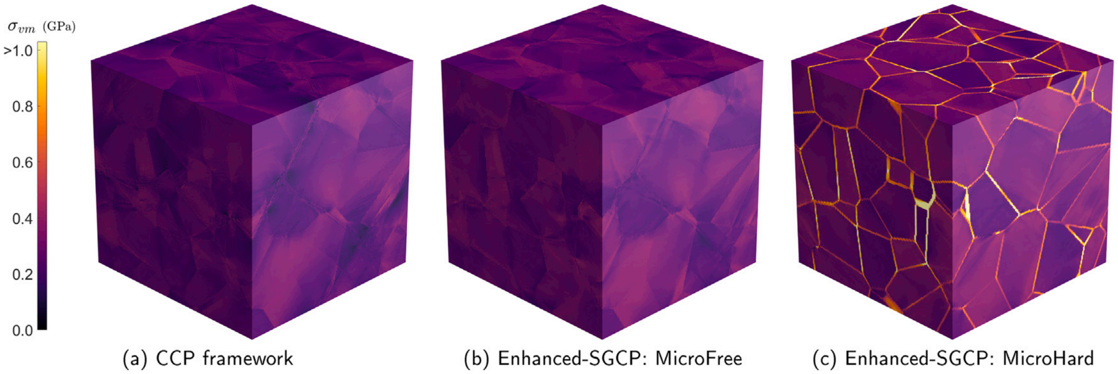

Fig. 17. Distributions of the von Mises stress, σ_{vm}, in the three-dimensional microstructure, obtained from the CCP framework and the Enhanced-SGCP theory with a length scale of $\Lambda_0 = 0.05$ mm and different higher-order interface conditions at the grain boundary at the end of applied loading, $\nabla u_{zz} = 0.01$.

the influence of strain gradient effects at higher deformation levels. In contrast, in the Classical-SGCP model, the length scale remains fixed throughout the loading process. This fundamental difference highlights a key divergence in the theoretical frameworks of the two models.

Furthermore, Fig. 19 presents the surface fraction with stress concentration at the grain boundaries for different higher-order interface conditions, following the procedure outlined in Fig. 9. The results indicate that stress concentration is more pronounced under the MicroHard condition in the Enhanced-SGCP theory compared to the Classical-SGCP model.

Fig. 20 presents the norm of the plastic distortion tensor and the rotation field for both the Classical-SGCP and Enhanced-SGCP theories under the MicroContinuity condition at the grain boundaries. The insets provide a detailed view of selected regions within the microstructure, highlighting key differences between the two theories. In the Classical-SGCP model, plastic deformation becomes more homogeneous within the grains, with a tendency disappearing of localized plastic deformation, indicating a loss of deformation heterogeneity. In contrast, in the Enhanced-SGCP theory, plastic deformation remains localized even at the final stage of loading, preserving the inherent microstructural characteristics such as the sweeping away the hardening defects inside the bands. Additionally, the insets depict a specific region of the microstructure that is further analyzed in Fig. 11 for different stages of the applied loading. In the Classical-SGCP model, plastic deformation within this region evolves more homogeneously over the course of loading, with no clear distinction between original slip bands and transferred slip bands. However, in the Enhanced-SGCP theory, localization is retained, and a clearer distinction between original slip bands and transferred slip bands emerges. Furthermore, in the Classical-SGCP model, also the rotation field loses its localization, resulting in a more homogeneous distribution within the grains. In contrast, in the Enhanced-SGCP theory, the rotation field remains localized and becomes more pronounced by the end of the loading process, reinforcing the influence of higher-order effects on plastic deformation. Therefore, it is concluded that the proposed Enhanced-SGCP theory successfully captures the evolution of microstructural features through the evolution of the higher-order stress during the deformation. This objective is achieved by linking the higher-order modulus, A^{α}, to the critical resolved shear stress, τ^{α}_{cr}, which serves as the central mechanism for representing the evolving microstructural state in irradiated crystals throughout the deformation process.

5. Conclusions

In this study, the Enhanced Strain Gradient Crystal Plasticity (Enhanced-SGCP) theory is introduced, incorporating the quadratic energy contribution of the Nye tensor. The theory introduces a physical length scale incorporated within the higher-order modulus, which is defined as a function of the microstructural properties of the lattice and evolves during applied loading. Consequently, the theory naturally leads to the derivation of back-stress and generalized back-stress in a thermodynamically consistent manner based on the Nye tensor. The proposed Enhanced-SGCP theory is applied to nonlinear softening behavior, successfully reproducing shear bands, which are widely reported in irradiated materials. In this framework, ideal slip and kink bands, representing two potential localization modes, are theoretically investigated. It is demonstrated that the Nye tensor corresponds to lattice curvature or lattice rotation, appearing only within kink bands, while slip bands remain free of rotational effects. Therefore, within the proposed theory, back-stress and generalized back-stress vanish in slip bands, whereas they remain nonzero in kink bands due to their intrinsic link with lattice curvature. This crucial distinction highlights the Enhanced-SGCP theory's capability to distinguish between slip and kink bands in a physically meaningful manner.

To further investigate the behavior of ideal kink bands, the Classical-SGCP theory (a Gurtin-type nonlocal theory) is initially implemented for computational simulations. However, the results reveal several numerical instabilities: (i) multiple non-regularized slip bands emerge within the kink bands, (ii) the width of the kink bands increases unrealistically during loading, ultimately leading to homogeneous deformation and loss of localization, (iii) the spacing between transferred slip bands is unstable and limited to a single-voxel width, and (iv) the number of transferred slip bands becomes voxel-dependent. Addressing these limitations is a primary objective of this study. The results obtained from the Enhanced-SGCP theory successfully resolve all numerical instabilities observed

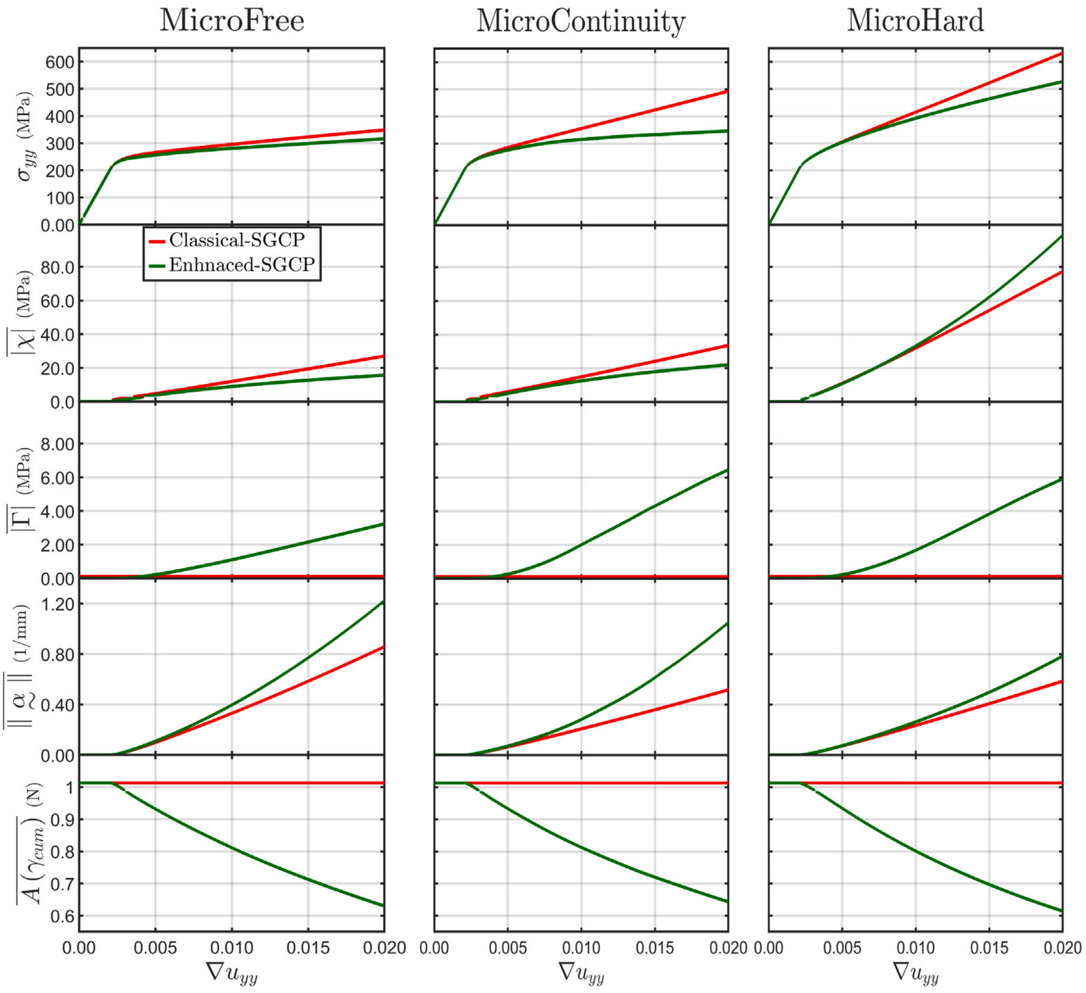

Fig. 18. Evolution of the spatially averaged tensile component of the Cauchy stress, σ_{yy}, along with the back-stress, $\overline{|\chi|}$, generalized back-stress, $\overline{|\Gamma|}$, norm of the Nye tensor, $\overline{\|\underset{\sim}{\alpha}\|}$, and higher-order modulus, $\overline{A(\gamma_{cum})}$, during applied loading. The results are obtained from the Classical-SGCP model with a length scale of $A = 1.01\ N$ and the Enhanced-SGCP theory with a length scale of $\Lambda_0 = 0.2$ mm, considering different higher-order interface conditions at the grain boundary.

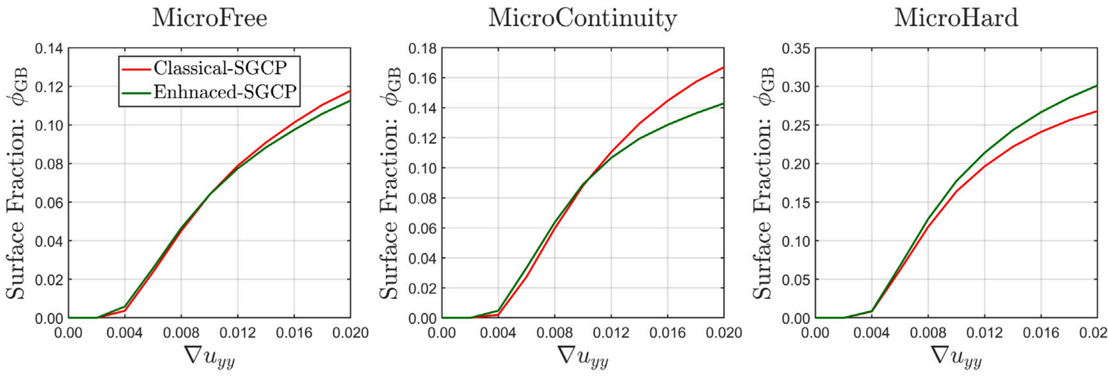

Fig. 19. Evolution of the surface fraction of grain boundaries with stress concentration, in the two-dimensional microstructure during applied loading, highlighting regions where the von Mises stress is concentrated along the grain boundaries. The results are obtained from the Classical-SGCP model with a length scale of $A = 1.01\ N$ and the Enhanced-SGCP theory with a length scale of $\Lambda_0 = 0.2$ mm, considering different higher-order interface conditions at the grain boundary.

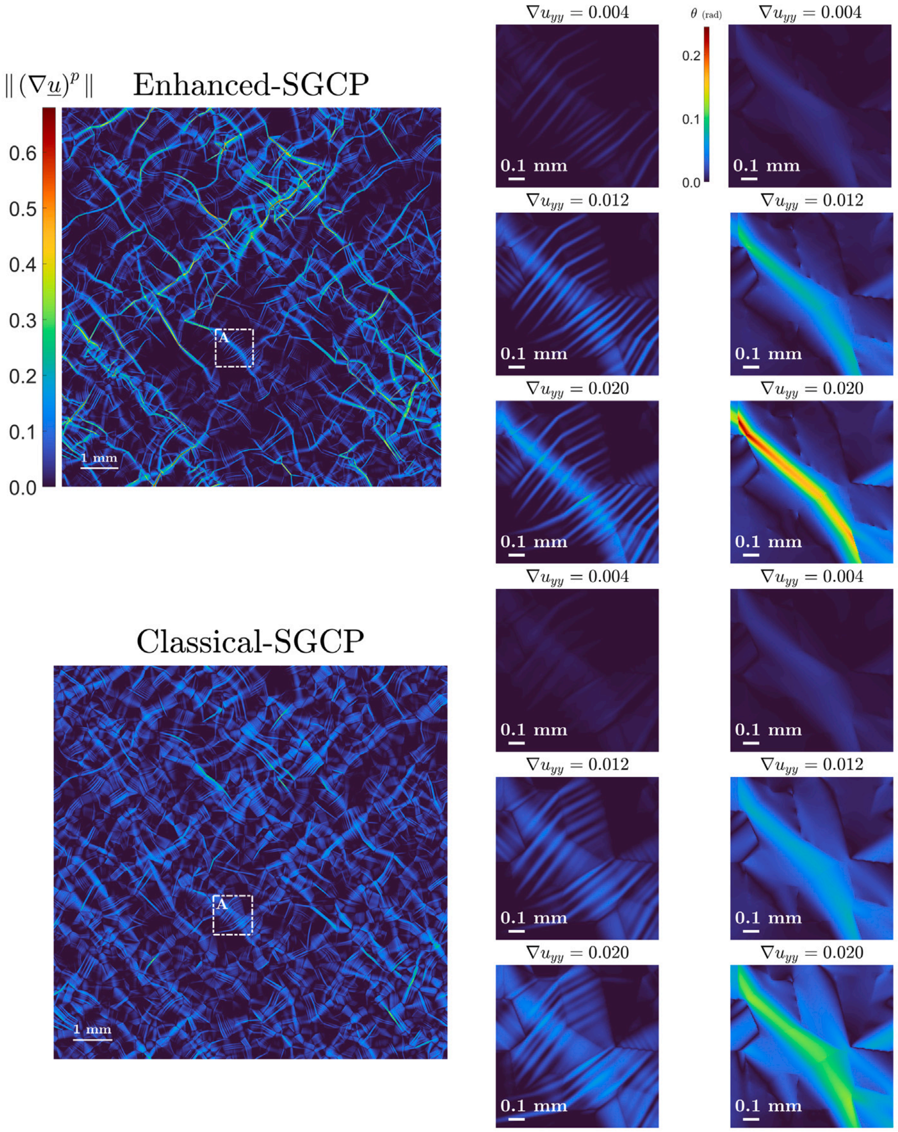

Fig. 20. Distributions of the norm of the plastic distortion tensor, $\|(\nabla \underline{u})^p\|$, and the rotation field, θ, in the two-dimensional microstructure at final stage of deformation ($\nabla u_{yy} = 0.02$), obtained from the Enhanced-SGCP theory with a length scale of $\Lambda_0 = 0.2$ mm and the Classical-SGCP model with a length scale of $A = 1.01\ N$ under the MicroContinuity condition at the grain boundary. The insets highlight a specific region of the microstructure same as in Fig. 10, illustrating the evolution of these distributions at three loading steps: $\nabla u_{yy} = 0.004$, $\nabla u_{yy} = 0.012$, and $\nabla u_{yy} = 0.02$.

in the Classical-SGCP theory. First, kink bands are replaced by regularized slip bands, which form ellipsoidal structures rather than being constrained to a single-voxel width. Second, the width of kink band is directly controlled by the length scale introduced within the theory, preventing fictitious growth and ensuring sustained localization during loading. Third, the spacing between transferred slip bands within the kink bands becomes smooth and well-regularized. Lastly, simulations conducted at varying length scales reveal that increasing the length scale leads to wider kink bands while reducing the number of transferred slip bands, demonstrating the theory's capability to consistently predict strain localization behavior.

Another key advancement of this study stands in the computational framework, which employs a fixed-point FFT method to solve the governing balance equations of both the Enhanced-SGCP and Classical-SGCP theories. To validate the accuracy of the FFT algorithm, an analytical solution for the ideal kink bands is derived within the Enhanced-SGCP framework. A comparison between the analytical solution and FFT-based numerical results shows excellent agreement, confirming the high accuracy and robustness of the FFT implementation in solving complex balance equations.

Furthermore, the proposed FFT algorithm is utilized to conduct high-resolution simulations of two-dimensional and three-dimensional polycrystalline aggregates under different higher-order interface conditions at the grain boundaries and varying length scales. A comparative analysis between the Conventional Crystal Plasticity (CCP) framework and the Enhanced-SGCP theory reveals that the latter induces additional hardening due to the accumulation of geometrically necessary dislocations (GNDs) evaluated by the Nye tensor. Additionally, comparisons between the Classical-SGCP and Enhanced-SGCP theories indicate that the additional hardening from GNDs in the Enhanced-SGCP model stabilizes and saturates at higher loading levels, ensuring sustained localization while limiting the effects of strain gradient plasticity (SGP). In contrast, the Classical-SGCP model exhibits a monotonically increasing hardening effect, ultimately leading to the loss of localization at high loading levels due to excessive strain gradient effects. The study also provides a comprehensive investigation into the role of grain boundaries. It is demonstrated that under the MicroHard condition, shear bands interacting with grain boundaries result in GND accumulation at these interfaces. This accumulation is accordingly suggested as the potential for micro-crack initiation in these regions, particularly in irradiated material with oxidized grain boundaries (IASCC).

In conclusion, the proposed Enhanced-SGCP theory, coupled with an efficient FFT-based numerical approach, represents a significant advancement over existing strain gradient crystal plasticity models. The framework successfully addresses critical challenges related to shear band localization, softening behavior, and numerical instabilities inherent in classical theories. Future developments will extend this approach toward large-deformation frameworks and explore hydrogen diffusion along slip and kink bands in irradiated materials. In parallel, efforts will focus on designing and conducting targeted experimental tests for calibrating material parameters in the irradiated single crystals. Moreover, special attention will be given to analyzing the transmission of shear bands across grain boundaries in the irradiated polycrystalline aggregates and incorporating the Electron Backscatter Diffraction images of the actual microstructure within the FFT method. These enhancements aim to deepen the predictive capabilities of the Enhanced-SGCP theory across a broader range of microstructural and loading conditions.

CRediT authorship contribution statement

Amirhossein Lame Jouybari: Writing – review & editing, Writing – original draft, Visualization, Validation, Software, Methodology, Investigation, Formal analysis, Data curation, Conceptualization. **Samir El Shawish:** Writing – review & editing, Writing – original draft, Visualization, Supervision, Investigation, Formal analysis, Resources. **Leon Cizelj:** Writing – review & editing, Supervision, Project administration, Investigation.

Declaration of competing interest

The authors declare that they have no known competing financial interests or personal relationships that could have appeared to influence the work reported in this paper.

Acknowledgment

The authors gratefully acknowledge the financial support provided by Slovenian Research and Innovation Agency (grants P2-0026 and young researcher Amirhossein Lame Jouybari).

Appendix A. Link between the Nye tensor and curl of plastic part of deformation

In continuum solid mechanics, the total deformation gradient tensor is a compatible field, which implies that the curl of the total deformation gradient tensor is zero.

$$\underset{\sim}{F}^{tot} = \underset{\sim}{1} + \nabla \underline{u}^{tot} \Rightarrow \nabla \times \left(\underset{\sim}{F}^{tot}\right) = \underset{\sim}{0} \tag{A.1}$$

However, based on the multiplicative decomposition of the total deformation gradient tensor, the elastic and plastic parts of the deformation gradient tensor do not necessarily form compatible tensor fields. As a result, the curl of these tensors does not vanish. Consequently, the dislocation density vector, $\underline{B}$, can be defined by applying a closed integral over one of these tensors for an oriented surface, $\mathcal{S}$, with a closed contour, $\mathcal{L}$, and normal vector $\underline{n}$, as expressed using Stokes' theorem: (Cermelli and Gurtin, 2002; Marano et al., 2021)

$$\underline{B} = \oint_{\mathcal{L}} \underset{\sim}{F}^{e-1} . d\underline{x} = -\int_{\mathcal{S}} \nabla \times \left(\underset{\sim}{F}^{e-1}\right) . \underline{n}\; dS \tag{A.2}$$

In general, the Burgers vector associated with a dislocation can be defined as the primary opening displacement of the closed contour, $\mathcal{L}$, as a result of the dislocations passing through the oriented surface, $\mathcal{S}$. Thus, the vector $\underline{B}$, as defined in Eq. (A.2), is able to represent the total Burgers vector of the closed contour, $\mathcal{L}$. Consequently, the curl of $\underset{\sim}{F}^{e-1}$ can be interpreted as the contribution from all GNDs passing through the oriented surface, $\mathcal{S}$, which leads to the definition of the Nye tensor, or the dislocation density tensor.

$$\underset{\sim}{\alpha} = -\nabla \times \left(\underset{\sim}{F}^{e-1}\right) \tag{A.3}$$

In the framework of the infinitesimal deformation, the Nye tensor can be further simplified by considering the additive decomposition of the total deformation gradient tensor into elastic and plastic parts of the displacement gradient tensors, Eq. (1).

$$\underset{\sim}{F}^{e-1} \simeq \underset{\sim}{1} - \left(\nabla \underline{u}\right)^{e} \tag{A.4}$$

$$\nabla \times \underset{\sim}{F}^{tot} = \nabla \times \left(\underset{\sim}{1} + \left(\nabla \underline{u}\right)^{e} + \left(\nabla \underline{u}\right)^{p}\right) = \nabla \times \left(\nabla \underline{u}\right)^{e} + \nabla \times \left(\nabla \underline{u}\right)^{p} = \underset{\sim}{0} \tag{A.5}$$

Therefore, by substituting Eqs. (A.4) and (A.5) into Eq. (A.3), the new expression for the Nye tensor is derived.

$$\underset{\sim}{\alpha} = \nabla \times \left(\nabla \underline{u}\right)^{e} = -\nabla \times \left(\nabla \underline{u}\right)^{p} \tag{A.6}$$

Appendix B. Correlation between Nye tensor, lattice curvature and the rotation field of the kink band

The elastic part of deformation gradient tensor can be multiplicatively decomposed into the rotation field ($\underset{\sim}{R}^{e}$) and right stretch tensor ($\underset{\sim}{U}^{e}$) using polar decomposition. Therefore, the Nye tensor in the kink band can be expressed by substituting the polar decomposition in Eq. (A.3):

$$\underset{\sim}{\alpha} = -\nabla \times \left(\underset{\sim}{F}^{e-1}\right) = -\nabla \times \left(\underset{\sim}{U}^{e-1}\underset{\sim}{R}^{e-1}\right) \tag{B.1}$$

In the infinitesimal deformation framework, assuming that the elastic stretch is much smaller compared to the localized plastic deformation and rotation field inside the kink band, the Nye tensor can be further simplified to: (Forest et al., 2019)

$$\underset{\sim}{\alpha} \simeq -\nabla \times \left(\underset{\sim}{R}^{e-1}\right) = -\nabla \times \left(\underset{\sim}{R}^{eT}\right) \tag{B.2}$$

Furthermore, by considering that the rotation field in the infinitesimal deformation framework is also small, the rotation field can be simplified with the skew-symmetric part of the displacement gradient tensor (Skew $\left(\nabla \underline{u}\right)^{e} = \underset{\sim}{\omega}^{e}$):

$$\underset{\sim}{\alpha} \simeq -\nabla \times \left(\underset{\sim}{R}^{e-1}\right) \simeq -\nabla \times \left(\underset{\sim}{1} - \underset{\sim}{\omega}^{e}\right) = \nabla \times \underset{\sim}{\omega}^{e} \tag{B.3}$$

Accordingly, as $\underset{\sim}{\omega}^{e}$ is a skew-symmetric tensor, an axial vector can be assigned:

$$\overset{\times}{\underline{\omega}} = -\frac{1}{2}\underset{\simeq}{\epsilon} : \underset{\sim}{\omega}^{e} \tag{B.4}$$

The corresponding angle, θ, associated to this rotation field, can be obtained (for the kink band) by the following expression.

$$\theta = \|\overset{\times}{\underline{\omega}}\| \tag{B.5}$$

Furthermore, in the framework of the infinitesimal deformation, the lattice curvature tensor can be defined by the gradient of the axial vector.

$$\underset{\sim}{\kappa} = \nabla \overset{\times}{\underline{\omega}} \tag{B.6}$$

Recalling the traditional formulation of the Nye tensor (Nye, 1953).

$$\underset{\sim}{\alpha} = \underset{\sim}{\kappa}^{T} - \mathrm{Tr}\left(\underset{\sim}{\kappa}\right)\underset{\sim}{1} \tag{B.7}$$

Provides the following matrix representation in the Cartesian coordinate system:

$$\left[\underset{\sim}{\alpha}\right] = \begin{bmatrix} -\overset{\times}{\omega}_{3,3} - \overset{\times}{\omega}_{2,2} & \overset{\times}{\omega}_{2,1} & \overset{\times}{\omega}_{3,1} \\ \overset{\times}{\omega}_{1,2} & -\overset{\times}{\omega}_{3,3} - \overset{\times}{\omega}_{1,1} & \overset{\times}{\omega}_{3,2} \\ \overset{\times}{\omega}_{1,3} & \overset{\times}{\omega}_{2,3} & -\overset{\times}{\omega}_{1,1} - \overset{\times}{\omega}_{2,2} \end{bmatrix} \tag{B.8}$$

Similarly, the matrix representation of the new formulation of the Nye tensor, Eq. (B.3), is written as:

$$\left[\underset{\sim}{\alpha}\right] = \left[\nabla \times \underset{\sim}{\omega}^{e}\right] = \left[\nabla \times \left(-\underset{\simeq}{\epsilon}.\overset{\times}{\underline{\omega}}\right)\right] = \begin{bmatrix} -\overset{\times}{\omega}_{3,3} - \overset{\times}{\omega}_{2,2} & \overset{\times}{\omega}_{2,1} & \overset{\times}{\omega}_{3,1} \\ \overset{\times}{\omega}_{1,2} & -\overset{\times}{\omega}_{3,3} - \overset{\times}{\omega}_{1,1} & \overset{\times}{\omega}_{3,2} \\ \overset{\times}{\omega}_{1,3} & \overset{\times}{\omega}_{2,3} & -\overset{\times}{\omega}_{1,1} - \overset{\times}{\omega}_{2,2} \end{bmatrix} \tag{B.9}$$

Since both matrix representations are the same, it is concluded that the traditional formulation of the Nye tensor is equal to the new definition given in Eq. (B.3) under certain assumptions.

Appendix C. Finite difference scheme

Consider a general scalar-valued function $A(x_1, x_2, x_3)$ defined in a three-dimensional real space. The Fourier transform of this function is denoted as $\hat{A}(\xi_1, \xi_2, \xi_3)$. One of the key properties of the Fourier space, which makes the FFT method computationally efficient, is that the partial derivative of the scalar-valued function with respect to the real space coordinates can be computed in Fourier space. This is achieved by multiplying the corresponding frequency-domain representation of the partial derivative K_i and the imaginary unit j, as shown in the following equation:

$$(\nabla A)_i = \mathcal{IFFT}\left(\mathrm{j}\hat{A}K_i\right) \tag{C.1}$$

Various finite difference schemes can be used to define the frequency-domain representation of the partial derivative. In this study, the 21-voxel finite difference scheme (FDS) for the two-dimensional case, or the 63-voxel FDS for the three-dimensional simulation, are considered. This scheme significantly enhances the accuracy (see (Neumann et al., 2002; Lame Jouybari et al., 2024)). Based on these FDS schemes, the frequency-domain representation of the partial derivative in Fourier space is introduced as follows:

$$K_i = \frac{1}{6dx_i}\left[-\sin(2\xi_i) + 8\sin(\xi_i)\right] \tag{C.2}$$

Using the 21-voxel or 63-voxel FDS, the frequency-domain representations of the gradient and curl operators for a second-order tensor $\underset{\sim}{A}$ are defined as:

$$\left(\nabla \underset{\sim}{A}\right)_{ijk} = \mathcal{IFFT}\left(A_{ij}K_j\right) = \mathcal{IFFT}\left(\widehat{\text{Grad}}\left(\underset{\sim}{\hat{A}}\right)\right) \tag{C.3}$$

$$\left(\nabla \times \underset{\sim}{A}\right)_{ij} = \mathcal{IFFT}\left(\epsilon_{jml}K_l\hat{A}_{im}\right) = \mathcal{IFFT}\left(\widehat{\text{Curl}}\left(\underset{\sim}{\hat{A}}\right)\right) \tag{C.4}$$

Similarly, using the 21-voxel or 63-voxel FDS, the second derivative of the scalar-valued function $A(x_1, x_2, x_3)$ can be obtained as:

$$\frac{\partial^2 A}{\partial x_i \partial x_j} = \mathcal{IFFT}\left(\hat{A}K_{ij}\right) \tag{C.5}$$

The frequency corresponding to the second derivative is given by: (Neumann et al., 2002)

$$K_{ij} = \begin{cases} \frac{2}{6dx_i^2}\left[-\cos(2\xi_i) + 16\cos(\xi_i) - 15\right] & \text{if } i = j \\ \frac{1}{2dx_i\,dx_j}\left[-\cos(\xi_i+\xi_j) - \cos(\xi_i+2\xi_j) + 10\cos(\xi_i+\xi_j) - 10\cos(-\xi_i+2\xi_j) + \cos(2\xi_i-\xi_j) + \cos(-\xi_i+2\xi_j)\right] & \text{if } i \neq j \end{cases} \tag{C.6}$$

Finally, the gradient-divergence and Laplacian operators for the second-order tensor-valued function are expressed as follows:

$$\left(\nabla \otimes \nabla \cdot \left(\underset{\sim}{A}\right)\right)_{ij} = \mathcal{IFFT}\left(\hat{A}_{im}K_{mj}\right) = \mathcal{IFFT}\left(\widehat{\text{Grad-Div}}\left(\underset{\sim}{\hat{A}}\right)\right) \tag{C.7}$$

$$\left(\Delta\left(\underset{\sim}{A}\right)\right)_{ii} = \mathcal{IFFT}\left(\hat{A}_{ii}K_{ii}\right) = \mathcal{IFFT}\left(\widehat{\text{Lap}}\left(\underset{\sim}{\hat{A}}\right)\right) \tag{C.8}$$

Appendix D. Implicit time integration

In the application of implicit time integration within the Enhanced-SGCP theory, the linear elastic strain ($\underset{\sim}{\varepsilon}^{\mathrm{e}}$) and the shear strain associated with each slip system (γ^α) are considered as the integration variables. In total, 18 increments are unknown for each voxel of the microstructure. Assuming that the total displacement gradient tensor field at the current time step, $\nabla\underline{u}^{tot}(t_n + \Delta t)$, and the state variables at the previous time step, t_n, are known, the residuals and their partial derivatives can be derived as follows:

$$R_{\underset{\sim}{\varepsilon}^e} = \Delta\underset{\sim}{\varepsilon}^e + \underset{\sim}{\varepsilon}^e(t_n) - \text{sym}\left(\nabla\underline{u}^{tot}(t_n + \Delta t)\right) + \underset{\sim}{\varepsilon}^p(t_n) + \sum_\alpha \Delta\gamma^\alpha\ \text{sym}(\underline{s}^\alpha \otimes \underline{m}^\alpha) \tag{D.1}$$

$$R_{\gamma^\alpha} = \Delta\gamma^\alpha - \Delta t\ \left\langle \frac{|\tau^\alpha - \chi^\alpha - \Gamma^\alpha| - \tau^\alpha_{cr}}{K} \right\rangle^n \text{sign}\left(\tau^\alpha - \chi^\alpha - \Gamma^\alpha\right) \tag{D.2}$$

$$\left(\frac{\partial R_{\underset{\sim}{\varepsilon}^e}}{\partial\Delta\underset{\sim}{\varepsilon}^e}\right)_{ijkl} = \frac{1}{2}\left[\delta_{ik}\delta_{jl} + \delta_{il}\delta_{jk}\right] \tag{D.3}$$

$$\frac{\partial R_{\underset{\sim}{\varepsilon}^e}}{\partial\Delta\gamma^\alpha} = \text{sym}(\underline{s}^\alpha \otimes \underline{m}^\alpha) \tag{D.4}$$

$$\frac{\partial R_{\gamma^\alpha}}{\partial\Delta\underset{\sim}{\varepsilon}^e} = -\Delta t\,\tfrac{n}{k}\left\langle \frac{|\tau^\alpha - \chi^\alpha - \Gamma^\alpha| - \tau^\alpha_{cr}}{K} \right\rangle^{\text{n-1}} \text{sym}(\underline{s}^\alpha \otimes \underline{m}^\alpha) : \underset{\approx}{C} \tag{D.5}$$

$$\frac{\partial R_{\gamma^\alpha}}{\partial\Delta\gamma^\beta} = \delta_{\alpha\beta}\left(1 + \Delta t\ \text{sign}\left(\tau^\alpha\ \gamma^\alpha\right)\tfrac{n}{K}\left\langle \frac{|\tau^\alpha - \chi^\alpha - \Gamma^\alpha| - \tau^\alpha_{cr}}{K} \right\rangle^{\text{n-1}} \left[-\frac{\Delta\tau^\alpha\ \exp\left(-\frac{\gamma^\alpha_{\text{cum}}}{\gamma_0}\right)}{\gamma_0}\right]\right) \tag{D.6}$$

It is important to note that, during the operation of the implicit time integration, the back-stress and generalized back-stress from the Enhanced-SGCP model, χ^α and Γ^α, are assumed to remain constant. The increments for the linear elastic strain and the shear strain associated with each slip system are then obtained through the following procedure, which is repeated until the desired tolerance is reached.

$$\begin{bmatrix} \Delta\underset{\sim}{\varepsilon}^e \\ \Delta\gamma^\alpha \end{bmatrix} = \begin{bmatrix} \frac{\partial R_{\underset{\sim}{\varepsilon}^e}}{\partial\Delta\underset{\sim}{\varepsilon}^e} & \frac{\partial R_{\underset{\sim}{\varepsilon}^e}}{\partial\Delta\gamma^\alpha} \\ \frac{\partial R_{\gamma^\alpha}}{\partial\Delta\underset{\sim}{\varepsilon}^e} & \frac{\partial R_{\gamma^\alpha}}{\partial\Delta\gamma^\beta} \end{bmatrix}^{-1} \begin{bmatrix} -R_{\underset{\sim}{\varepsilon}^e} \\ -R_{\gamma^\alpha} \end{bmatrix} \tag{D.7}$$

In the case of the Classical-SGCP model, the same procedure is followed; however, the residual of the shear strain and its partial derivatives differ from those in the Enhanced-SGCP theory. These differences are outlined below.

$$R_{\gamma^\alpha} = \Delta\gamma^\alpha - \Delta t\ \left\langle \frac{|\tau^\alpha - \chi^\alpha| - \tau^\alpha_{cr}}{K} \right\rangle^n \text{sign}\left(\tau^\alpha - \chi^\alpha\right) \tag{D.8}$$

$$\frac{\partial R_{\gamma^\alpha}}{\partial \Delta \underset{\sim}{\varepsilon}^e} = -\Delta t \, \tfrac{n}{k} \left\langle \frac{|\tau^\alpha - \chi^\alpha| - \tau^\alpha_{cr}}{K} \right\rangle^{\text{n-1}} \text{sym}(\underline{s}^\alpha \otimes \underline{m}^\alpha) : \underset{\approx}{C} \tag{D.9}$$

$$\frac{\partial R_{\gamma^\alpha}}{\partial \Delta \gamma^\beta} = \delta_{\alpha\beta} \left(1 + \Delta t \ \text{sign}\left(\tau^\alpha \ \gamma^\alpha\right) \tfrac{n}{K} \left\langle \frac{|\tau^\alpha - \chi^\alpha| - \tau^\alpha_{cr}}{K} \right\rangle^{\text{n-1}} \left[- \frac{\Delta \tau^\alpha \ \exp\left(-\frac{\gamma^\alpha_{\text{cum}}}{\gamma_0}\right)}{\gamma_0} \right] \right) \tag{D.10}$$

Appendix E. Threshold criterion for length scale

In all polycrystalline simulations, a threshold-based criterion is employed to select an appropriate length scale Λ_0 relative to the mean grain size (GS). This selection is crucial to ensure that the influence of the Enhanced-SGCP theory is physically meaningful. The relation between the intrinsic length scale and the grain size is interpreted as follows:

- **If** $\Lambda_0 \ll$ GS: The influence of the Enhanced-SGCP theory becomes negligible. In this regime, the width of the transferred slip bands (original kink bands) is significantly smaller than the grain size and original slip bands, resulting in a limited activation of higher-order effects. Consequently, the associated higher-order modulus A^α — which scales and weights the back-stress and generalized back-stress — remains small and has minimal impact on the material response.
- **If** $\Lambda_0 \leq$ GS: The Enhanced-SGCP theory operates within an appropriate range. Here, the width of the transferred slip bands from kink band is smaller than the grain size, ensuring that the strain gradient effects are confined to intragranular regions, consistent with physical expectations.
- **If** $\Lambda_0 >$ GS: The influence of the Enhanced-SGCP theory becomes excessive and potentially overestimated. In this case, the width of the transferred slip bands from kink band may exceed the grain size, leading to unphysical interactions across grain boundaries and unrealistic contributions from higher-order stress terms with respect to the softening terms which causing in eliminating plastic deformation and achieving a purely elastic response.

This threshold-based interpretation helps guide the selection of Λ_0 to maintain the physical accuracy and computational stability of the simulations.

Data availability

Data will be made available on request.

References

Abatour, M., Forest, S., 2024. Strain gradient plasticity based on saturating variables. Eur. J. Mech. A Solids 104, 105016.

Agius, D., Kareer, A., Al Mamun, A., Truman, C., Collins, D.M., Mostafavi, M., Knowles, D., 2022. A crystal plasticity model that accounts for grain size effects and slip system interactions on the deformation of austenitic stainless steels. Int. J. Plast. 152, 103249.

Ahmadikia, B., Kumar, M.A., Beyerlein, I.J., 2021. Effect of neighboring grain orientation on strain localization in slip bands in HCP materials. Int. J. Plast. 144, 103026.

Aifantis, E.C., 1984. On the microstructural origin of certain inelastic models. ASME 106, 326–330.

Asaro, R., Rice, J., 1977. Strain localization in ductile single crystals. J. Mech. Phys. Solids 25 (5), 309–338.

Cermelli, P., Gurtin, M.E., 2002. Geometrically necessary dislocations in viscoplastic single crystals and bicrystals undergoing small deformations. Int. J. Solids Struct. 39 (26), 6281–6309.

Clayton, J.D., 2022. Modeling deformation and fracture of boron-based ceramics with nonuniform grain and phase boundaries and thermal-residual stress. Solids 3 (4), 643–664.

Clayton, J.D., 2024. Analysis of shear localization in viscoplastic solids with pressure-sensitive structural transformations. J. Mech. Phys. Solids 193, 105880.

Clayton, J.D., McDowell, D.L., Bammann, D.J., 2004. A multiscale gradient theory for single crystalline elastoviscoplasticity. Internat. J. Engrg. Sci. 42 (5-6), 427–457.

Dahlberg, C., Boasen, M., 2019. Evolution of the length scale in strain gradient plasticity. Int. J. Plast. 112, 220–241.

Demir, E., Horton, E.W., Kareer, A., Collins, D.M., Mostafavi, M., Knowles, D., 2023. A finite element method to calculate geometrically necessary dislocation density: Accounting for orientation discontinuities in polycrystals. Acta Mater. 245, 118658.

Fleck, N.A., Hutchinson, J.W., 1997. Strain gradient plasticity. Adv. Appl. Mech. 33, 295–361.

Fleck, N., Muller, G., Ashby, M., Hutchinson, J., 1994. Strain gradient plasticity - theory and experiment. Acta Metall. Mater. 42, 475–487.

Forest, S., 1998. Modeling slip, kink and shear banding in classical and generalized single crystal plasticity. Acta Mater. 46, 3265–3281.

Forest, S., Mayeur, J., McDowell, D., 2019. Micromorphic crystal plasticity. In: Voyiadjis, G. (Ed.), Handbook of Nonlocal Continuum Mechanics for Materials and Structures. Springer, pp. 643–686.

Gao, H., Huang, Y., Nix, W., Hutchinson, J., 1999. Mechanism-based strain gradient plasticity—I. Theory.. J. Mech. Phys. Solids 47, 1239–1263.

Gracio, J., 1994. The double effect of grain-size on the work-hardening behavior of polycrystalline copper. Scr. Metall. Mater. 31, 487–489.

Gudmundson, P., 2004. A unified treatment of strain gradient plasticity. J. Mech. Phys. Solids 52, 1379–1406.

Gurtin, M.E., 2002. A gradient theory of single-crystal viscoplasticity that accounts for geometrically necessary dislocations. J. Mech. Phys. Solids 50 (1), 5–32.

Gurtin, M., Anand, L., 2005. A theory of strain-gradient plasticity for isotropic, plastically irrotational materials. Part I: Small deformations. J. Mech. Phys. Solids 53, 1624–1649.

Hall, E.O., 1951. The deformation and ageing of mild steel: discussion of results. Proc. Phys. Soc. Section B 64 (9), 747.

Hassani, R., Ansari, R., Basti, A., 2025. Dynamic analysis of 2D micromorphic hyperelastic continua considering finite deformation: a novel numerical approach. Appl. Math. Model. 115941.

Hestroffer, J.M., Stinville, J.C., Charpagne, M.A., Miller, M.P., Pollock, T.M., Beyerlein, I.J., 2023. Slip localization behavior at triple junctions in nickel-base superalloys. Acta Mater. 249, 118801.

Hure, J., El Shawish, S., Cizelj, L., Tanguy, B., 2016. Intergranular stress distributions in polycrystalline aggregates of irradiated stainless steel. J. Nucl. Mater. 476, 231–242.

Kröner, E., 1962. Dislocations and continuum mechanics. Appl. Mech. Rev. 15 (8), 599–606.

Lame Jouybari, A., El Shawish, S., Cizelj, L., 2023. Crystal plasticity model of austenitic stainless steels subjected to hydrogen concentration and neutron irradiation. In: Proc. Int. Conf. Nucl. Eng. Vol. 30. ICONE, p. 1729.

Lame Jouybari, A., El Shawish, S., Cizelj, L., 2024. Fast Fourier transform approach to strain gradient crystal plasticity: Regularization of strain localization and size effect. Int. J. Plast. 183, 104153.

Lindroos, M., Pinomaa, T., Ammar, K., Laukkanen, A., Provatas, N., Forest, S., 2022a. Dislocation density in cellular rapid solidification using phase field modeling and crystal plasticity. Int. J. Plast. 148, 103139.

Lindroos, M., Scherer, J., Forest, S., Laukkanen, A., Andersson, T., Vaara, J., Mäntylä, A., Frondelius, T., 2022b. Micromorphic crystal plasticity approach to damage regularization and size effects in martensitic steels. Int. J. Plast. 151, 103187.

Ling, C., Forest, S., Besson, J., Tanguy, B., Latourte, F., 2018. A reduced micromorphic single crystal plasticity model at finite deformations. Application to strain localization and void growth in ductile metals. Int. J. Solids Struct. 134, 43–69.

Lippmann, B.A., Schwinger, J., 1950. Variational principles for scattering processes. Phys. Rev. 79 (3), 469.

Liu, D., Dunstan, D.J., 2017. Material length scale of strain gradient plasticity: A physical interpretation. Int. J. Plast. 98, 156–174.

Lucarini, S., Segurado, J., 2019. An algorithm for stress and mixed control in Galerkin-based FFT homogenization. Internat. J. Numer. Methods Engrg. 119, 797–805.

Lucarini, S., Upadhyay, M.V., Segurado, J., 2021. FFT based approaches in micromechanics: fundamentals, methods and applications. Modelling Simul. Mater. Sci. Eng. 30 (2), 023002.

Mahajan, S., Eyre, B.L., 2017. Formation of dislocation channels in neutron irradiated molybdenum. Acta Mater. 122, 259–265.

Marano, A., Gélébart, L., Forest, S., 2019. Intragranular localization induced by softening crystal plasticity: Analysis of slip and kink bands localization modes from high resolution FFT-simulations results. Acta Mater. 175, 262–275.

Marano, A., Gélébart, L., Forest, S., 2021. FFT-based simulations of slip and kink bands formation in 3D polycrystals: Influence of strain gradient crystal plasticity. J. Mech. Phys. Solids 149, 104295.

Matlab, R., 2022. Release, S. T. 2022a. The MathWorks, Inc., Natick, Massachusetts, United States.

McMurtrey, M., Was, G., Patrick, L., Farkas, D., 2011. Relationship between localized strain and irradiation assisted stress corrosion cracking in an austenitic alloy. Mater. Sci. Eng. 528, 3730–3740.

Michel, J.C., Moulinec, H., Suquet, P., 1999. Effective properties of composite materials with periodic microstructure: a computational approach. Comput. Methods Appl. Mech. Engrg. 172 (1-4), 109–143.

Moulinec, H., Suquet, P., 1998. A numerical method for computing the overall response of nonlinear composites with complex microstructure. Comput. Methods Appl. Mech. Engrg. 157 (1-2), 69–94.

Neumann, S., Herrmann, K.P., Müller, W.H., 2002. Stress/strain computation in heterogeneous bodies with discrete Fourier transforms—-different approaches. Comput. Mater. Sci. 25 (1-2), 151–158.

Nye, J.F., 1953. Some geometrical relations in dislocated crystals. Acta Metall. 1 (2), 153–162.

Pai, N., Prakash, A., Samajdar, I., Patra, A., 2022. Study of grain boundary orientation gradients through combined experiments and strain gradient crystal plasticity modeling. Int. J. Plast. 156, 103360.

Patra, A., McDowell, D.L., 2016. Crystal plasticity investigation of the microstructural factors influencing dislocation channeling in a model irradiated bcc material. Acta Mater. 110, 364–376.

Petch, N.J., 1953. The cleavage strength of polycrystals. Iron Steel Inst. 174, 25–28.

Petryk, H., Stupkiewicz, S., 2016. A minimal gradient-enhancement of the classical continuum theory of crystal plasticity. Part I: the hardening law. Arch. Mech. 68, 459–485.

Phalke, V., Forest, S., Chang, H.J., Roos, A., 2022a. Adiabatic shear banding in FCC metallic single and poly-crystals using a micromorphic crystal plasticity approach. Mech. Mater. 169, 104288.

Phalke, V., Kaiser, T., Scherer, J.M., Forest, S., 2022b. Modeling size effects in microwire torsion: A comparison between a Lagrange multiplier-based and a curlfp gradient crystal plasticity model. Eur. J. Mech. A Solids 94, 104550.

Poh, L., Sun, G., 2017. Localizing gradient damage model with decreasing interactions. Internat. J. Numer. Methods Engrg. 110, 503–522.

Prakash, A., Tak, T.N., Pai, N.N., Murty, S.N., Guruprasad, P.J., Doherty, R.D., Samajdar, I., 2021. Slip band formation in low and high solute aluminum: a combined experimental and modeling study. Modelling Simul. Mater. Sci. Eng. 29 (8), 085016.

Quey, R., Dawson, P.R., Barbe, F., 2011. Large-scale 3D random polycrystals for the finite element method: Generation, meshing and remeshing. Comput. Methods Appl. Mech. Engrg. 200 (17-20), 1729–1745.

Ramière, I., Helfer, T., 2015. Iterative residual-based vector methods to accelerate fixed point iterations. Comput. Math. Appl. 70 (9), 2210–2226.

Ren, S.C., Morgeneyer, T.F., Mazière, M., Forest, S., Rousselier, G., 2021. Effect of Lüders and portevin–le chatelier localization bands on plasticity and fracture of notched steel specimens studied by DIC and FE simulations. Int. J. Plast. 136, 102880.

Ryś, M., Stupkiewicz, S., Petryk, H., 2022. Micropolar regularization of crystal plasticity with the gradient-enhanced incremental hardening law. Int. J. Plast. 156, 103355.

Scherer, J.M., Besson, J., Forest, S., Hure, J., Tanguy, B., 2019. Strain gradient crystal plasticity with evolving length scale: Application to voided irradiated materials. Eur. J. Mech. A Solids 77, 103768.

Scherer, J.M., Besson, J., Forest, S., Hure, J., Tanguy, B., 2021. A strain gradient plasticity model of porous single crystal ductile fracture. J. Mech. Phys. Solids 156, 104606.

Stolken, J., Evans, A., 1998. A microbend test method for measuring the plasticity length scale. Acta Mater. 46, 5109–5115.

Vandoren, B., Simone, A., 2018. Modeling and simulation of quasi-brittle failure with continuous anisotropic stress-based gradient-enhanced damage models. Comput. Methods Appl. Mech. Engrg. 332, 644–685.

Voyiadjis, G., Abu Al-Rub, R., 2005. Gradient plasticity theory with a variable length scale parameter. Int. J. Solids Struct. 42, 3998–4029.

Wicht, D., Schneider, M., Böhlke, T., 2021. Anderson-accelerated polarization schemes for fast Fourier transform-based computational homogenization. Internat. J. Numer. Methods Engrg. 122 (9), 2287–2311.

Willot, F., 2015. Fourier-based schemes for computing the mechanical response of composites with accurate local fields. C. R. Méc. 343 (3), 232–245.

Wulfinghoff, S., Bayerschen, E., Böhlke, T., 2013. A gradient plasticity grain boundary yield theory. Int. J. Plast. 51, 33–46.

Zbib, H., Aifantis, E., 1998. On the structure and width of shear bands. Scr. Met. 22, 703–708.